PHYSICAL REVIEW C **75**, 014902 (2007)

Space-time evolution of bulk QCD matter

Chiho Nonaka
Department of Physics, Nagoya University, Nagoya 464-8602, Japan, and
School of Physics and Astronomy, University of Minnesota, Minnesota 55455, USA

Steffen A. Bass
Department of Physics, Duke University, Durham, North Carolina 27708, USA
(Received 10 July 2006; published 5 January 2007)

We introduce a combined, fully three-dimensional macroscopic/microscopic transport approach employing relativistic 3D hydrodynamics for the early, dense, deconfined stage of the reaction and a microscopic nonequilibrium model for the later hadronic stage where the equilibrium assumptions are no longer valid. Within this approach, we study the dynamics of hot bulk QCD matter, which is being created in ultrarelativistic heavy-ion collisions at the BNL Relativistic Heavy-Ion Collider. Our work is an extension of the well-known hybrid macro+micro approach in 1+1 and 2+1 dimensions, which is capable of self-consistently calculating the freeze-out of the hadronic system while accounting for the collective flow on the hadronization hypersurface generated by the quark-gluon plasma expansion. In particular, we perform a detailed analysis of the reaction dynamics, hadronic freeze-out, and transverse flow.

DOI: 10.1103/PhysRevC.75.014902 PACS number(s): 25.75.−q, 24.10.Nz, 24.10.Lx

I. INTRODUCTION

A major goal of colliding heavy ions at relativistic energies is to heat up a small region of space-time to temperatures as high as those thought to have occurred during the early evolution of the universe, a few microseconds after the big bang [1]. In ultrarelativistic heavy-ion collisions, such as are currently being explored at the BNL Relativistic Heavy-Ion Collider (RHIC), the four-volume of hot dense matter, with temperatures above ∼150 MeV, is on the order of ∼10 fm^4. The state of strongly interacting matter at such high temperatures (or density of quanta) is usually called quark-gluon plasma (QGP) [2].

The first five years of RHIC operations at $\sqrt{s_{NN}} = 130$ and 200 GeV have yielded a vast amount of interesting and sometimes surprising results [3–5], many of which have not yet been fully evaluated or understood by theory. There exists mounting evidence that RHIC experiments have created a hot dense state of deconfined QCD matter with properties similar to those of an ideal fluid [6,7]—this state of matter has been termed the strongly interacting quark-gluon plasma (sQGP).

Heavy-ion collisions at RHIC involve several distinct reaction stages, starting with the two initial ground states of the colliding nuclei, followed by the high density phase in which a sQGP is formed, and ending with the final freeze-out of hadrons.

The central problem in studying the sQGP is that the deconfined quanta of a sQGP are not directly observable because of the fundamental confining property of the physical QCD vacuum. If we could see free quarks and gluons (as in ordinary plasmas) it would be trivial to verify the QCD prediction of the QGP state. However, nature chooses to hide those constituents within the confines of color neutral composite many-body systems—hadrons. One of the main tasks in relativistic heavy-ion research is to find clear and unambiguous connections between the transient (partonic) plasma state and the observable hadronic final state (for a review on QGP signatures, see [8]).

One particular approach to this problem is the application of transport theory. Transport theory ultimately aims at casting the entire time evolution of the heavy-ion reaction—from its initial state to freeze-out—into one consistent framework. By tuning the physical parameters of the transport calculation to data, one can then infer from these the properties of the hot dense QCD matter of the sQGP and compare these properties to the predictions made by lattice gauge theory (LGT).

II. SPECIFIC MODEL FOR HIGH-ENERGY HEAVY-ION COLLISIONS

Relativistic fluid dynamics (RFD, see, e.g., Refs. [9–11]) is ideally suited for the QGP and hydrodynamic expansion reaction phase, but it breaks down in the later, dilute stages of the reaction when the mean free paths of the hadrons become large and flavor degrees of freedom are important. The most important advantage of RFD is that it directly incorporates an equation of state (EoS) as input and thus is so far the only dynamic model in which a phase transition can explicitly be incorporated. In the ideal fluid approximation (i.e., neglecting off-equilibrium effects), and once an initial condition has been specified, the EoS is the *only* input to the equations of motion and relates directly to properties of the matter under consideration. The hydrodynamic description has been very successful [12–14] in describing the collective behavior of soft particle production at RHIC.

Conventional RFD calculations need to assume a freeze-out temperature at which the hydrodynamic evolution is terminated, and a transition from the zero mean-free-path approximation of a hydrodynamic approach to the infinite mean-free-path of free streaming particles takes place. The freeze-out temperature usually is a free parameter which (within reasonable constraints) can be fitted to measured hadron spectra.

The reach of RFD can be extended and the problem of having to terminate the calculation at a fixed freeze-out temperature can be overcome by combining the RFD calculation with a microscopic hadronic cascade model; this kind of hybrid approach (dubbed hydro plus micro) was pioneered in [15] and has been now also taken up by other groups [16,17]. Its key advantages are that the freeze-out now occurs naturally as a result of the microscopic evolution and that flavor degrees of freedom are treated explicitly through the hadronic cross sections of the microscopic transport. Because the Boltzmann equation is the basis of the microscopic calculation in the hadronic phase, viscous corrections for the hadronic phase are by default included in the approach.

Here, we combine the hydrodynamic approach with the microscopic ultrarelativistic quantum molecular dynamics (UrQMD) model [18], in order to provide an improved description of the later, purely hadronic stages of the reaction. Such hybrid macro/micro transport calculations are to date the most successful approaches for describing the soft physics at RHIC. The biggest advantage of the RFD part of the calculation is that it directly incorporates an equation of state as input; one of its largest limitations is that it requires thermalized initial conditions, and one is not able to do an *ab initio* calculation.

A. Hydrodynamics

In the present paper, we shall use a fully three-dimensional hydrodynamic model [19] for the description of RHIC physics, especially focusing on Au + Au collisions at RHIC energies ($\sqrt{s_{NN}} = 200$ GeV per nucleon-nucleon pair). Our original code for solving the hydrodynamic equations, which is based on Cartesian coordinates [19], has been modified to the description on the coordinate by longitudinal proper time $\tau = \sqrt{t^2 - z^2}$ and $\eta = \frac{1}{2}\ln[(t+z)/(t-z)]$, in order to optimize the hydrodynamic expressions for ultrarelativistic heavy-ion collisions.

In hydrodynamic models, the starting point is the relativistic hydrodynamic equation

$$\partial_\mu T^{\mu\nu} = 0, \tag{1}$$

where $T^{\mu\nu}$ is the energy momentum tensor given by

$$T^{\mu\nu} = (\epsilon + p)U^\mu U^\nu - p g^{\mu\nu}. \tag{2}$$

Here ϵ, p, U, and $g^{\mu\nu}$ are energy density, pressure, four-velocity, and metric tensor, respectively. We solve the relativistic hydrodynamic equation (1) numerically with baryon number n_B conservation

$$\partial_\mu (n_B(T,\mu)U^\mu) = 0. \tag{3}$$

To rewrite the relativistic hydrodynamic equation (1) in the coordinate (τ, x, y, η), we introduce the variables [20]

$$\begin{aligned}\tilde{v}_x &= v_x \cosh Y_L / \cosh(Y_L - \eta),\\ \tilde{v}_y &= v_y \cosh Y_L / \cosh(Y_L - \eta),\\ \tilde{v}_\eta &= \tanh(Y_L - \eta),\end{aligned} \tag{4}$$

where $Y_L = \frac{1}{2}\ln((1+v_z)/(1-v_z))$, $\eta = 1/2\ln((t+z)/(t-z))$. Equation (1) in the explicit way is rewritten in the Appendix.

To solve the relativistic hydrodynamic equations, we adopt Lagrangian hydrodynamics. In Lagrangian hydrodynamics, the coordinates of the individual cells do not remain fixed, but move along the flux of the fluid. In the absence of turbulence during the expansion, Lagrangian hydrodynamics has several advantages over the conventional Eulerian approach:

(i) Computational expediency: a fixed number of cells can be utilized through the entire calculation. A Lagrangian hydrodynamic code can thus easily be employed even at ultra-high-energy collisions such as at the CERN Large Hadron Collider (LHC) where a large difference of scale exists between the initial and final states because of the large γ factor and rapid expansion of the QCD matter.

(ii) Analysis efficiency: the adiabatic path of each volume element of fluid can be traced in the phase diagram, making it possible to directly discuss the effects of the phase transition on physical observables [19].

Our algorithm for solving the relativistic hydrodynamic equation in 3D is based on the conservation laws for entropy and baryon number. Further details concerning the numerical method can be found in Ref. [19].

B. Equation of state

To solve the relativistic hydrodynamic equation, an equation of state (EoS) needs to be specified. The inclusion of an equation of state as input is one of the biggest advantages of RFD, which is so far the only dynamic model in which a phase transition can explicitly be incorporated. In the ideal fluid approximation (i.e., neglecting off-equilibrium effects), the EoS is the *only* input to the equations of motion and relates directly to properties of the matter under consideration. Once the EoS has been fixed (e.g., through a lattice-QCD calculation) a comparison to data can be used to extract information on the initial conditions of the hydrodynamic calculation [21].

Lattice-QCD (lQCD) offers the only rigorous approach for determining the EoS of QCD matter. Calculations at vanishing baryon chemical potential suggest that for physical values of the quark masses [two light (u, d) quarks and a heavier s quark], the deconfinement transition is a rapid crossover rather than a first-order phase transition with singularities in the bulk thermodynamic observables [22]. The critical temperature at $\mu_B = 0$ for the rapid crossover in the (2+1) flavor case was recently predicted to be $T_c = 172 \pm 11$ MeV [23].

However, many QCD motivated calculations for low temperatures and high baryon densities exhibit a strong first-order phase transition (with a phase coexistence region) [24,25]. These two limiting cases suggest that there exists a critical point (second-order phase transition) [26] at the end point of a line of first-order phase transitions. Recently, the exploration of the phase diagram for large temperatures and small, but nonvanishing, values of the baryon chemical potential became possible through the application of novel techniques, such as Ferrenberg-Swendsen reweighting [27], Taylor series expansions [28,29], or simulations with an imaginary chemical potential [30,31]. Although these techniques have allowed considerable improvements, the location of the critical point in the T-μ_B plane still has large theoretical uncertainties, because of the sensitivity to the quark masses and the lattice sizes used in the calculations. The predicted values of $\mu_B^{\text{endpoint}}/T_c$ vary between 1 and 3 [32–34], i.e., $\mu_B^{\text{endpoint}} = 170$–$420$ MeV.

For the calculation presented in this work, we use a simple equation of state with the first-order phase transition, which will allow us to compare our results with those of previous hydrodynamic and hybrid calculations employing (1+1) dimensional [15] and (2+1) dimensional [16] hydrodynamic models.

Above the critical temperature ($T_c = 160$ MeV at $\mu = 0$ MeV), the thermodynamic quantities are assumed to be determined by a QGP which is dominated by massless u, d, s quarks and gluons. The pressure in QGP phase is given by

$$p_{\mathrm{Q}} = \frac{(32 + 21N_f)\pi^2}{180}T^4 + \frac{N_f}{2}\left(\frac{\mu}{3}\right)^2 T^2 + \frac{N_f}{4\pi^2}\left(\frac{\mu}{3}\right)^4 - B, \tag{5}$$

where N_f is 3 and B is the bag constant [35,36]. For the hadronic phase, we use a hadron gas equation of state with excluded volume correction [37]. Here, the pressure for fermions is given by

$$\begin{aligned} p_{\mathrm{H}}^{\text{excl}}(T, \{\mu_i\}) &= \sum_i p_i^{\text{ideal}}(T, \mu_i - V_0 p^{\text{excl}}(T, \{\mu_i\})) \\ &= \sum_i p_i^{\text{ideal}}(T, \tilde{\mu}_i), \end{aligned} \tag{6}$$

where p^{ideal} is the pressure of ideal hadron gas and V_0 is the excluded volume of hadrons whose radii are fixed to 0.7 fm. In the low-temperature region, the well-established (strange and nonstrange) hadrons up to masses of ~2 GeV are included in the EoS (see Tables I and II for a detailed listing). Although heavy states are rare in thermodynamic equilibrium, they have a larger entropy per particle than light states and therefore have considerable impact on the evolution. In particular, hadronization is significantly faster than in the case where the hadron gas consists of light mesons only (see the discussions in [35,38–42]).

The hadronic states used in the EoS of our hydrodynamic calculation are identical to those used in the microscopic model employed for the hadronic stage of the reaction (UrQMD, see Sec. II E). This is necessary to ensure consistency between the properties of the hadron gas in the hydrodynamic as well as in the microscopic picture and allows a smooth transition from one description to the other. UrQMD additionally assumes a continuum of color-singlet states called "strings" above the $m \simeq 2$ GeV threshold to model $2 \rightarrow n$ processes and inelastic processes at high c.m. energy. For example, the annihilation of an $\overline{p}$ on an Ω is described as excitation of two strings with the same quantum numbers as the incoming hadrons, respectively, which are subsequently mapped on known hadronic states according to a fragmentation scheme. Since we shall be interested in the dynamics of the Ω baryons emerging from the hadronization of the QGP, it is unavoidable that we treat string formation. The fact that string degrees of freedom are not taken into account in the EoS (6) does not represent a problem in our case since we focus on rapidly expanding systems where those degrees of freedom cannot equilibrate [43].

TABLE I. Baryons and baryon resonances treated in the model, and corresponding antibaryon states.

Nucleon	Delta	Lambda	Sigma	Xi	Omega
N_{938}	Δ_{1232}	Λ_{1116}	Σ_{1192}	Ξ_{1317}	Ω_{1672}
N_{1440}	Δ_{1600}	Λ_{1405}	Σ_{1385}	Ξ_{1530}	
N_{1520}	Δ_{1620}	Λ_{1520}	Σ_{1660}	Ξ_{1690}	
N_{1535}	Δ_{1700}	Λ_{1600}	Σ_{1670}	Ξ_{1820}	
N_{1650}	Δ_{1900}	Λ_{1670}	Σ_{1775}	Ξ_{1950}	
N_{1675}	Δ_{1905}	Λ_{1690}	Σ_{1790}		
N_{1680}	Δ_{1910}	Λ_{1800}	Σ_{1915}		
N_{1700}	Δ_{1920}	Λ_{1810}	Σ_{1940}		
N_{1710}	Δ_{1930}	Λ_{1820}	Σ_{2030}		
N_{1720}	Δ_{1950}	Λ_{1830}			
N_{1900}		Λ_{2100}			
N_{1990}		Λ_{2110}			
N_{2080}					
N_{2190}					
N_{2200}					
N_{2250}					

The phase coexistence region is constructed employing the Gibbs conditions of phase equilibrium. The bag parameter $B = 385$ MeV/fm^3 is chosen to yield the critical temperature $T_C = 160$ MeV at $\mu = 0$. In the coexistence region of the QGP and hadron phases (i.e., the mixed phase), we introduce the fraction of the volume of the QGP phase, $\lambda(x_\mu)$ $(0 \leqslant \lambda \leqslant 1)$ and parametrize energy density and baryon number density as

$$\begin{aligned} \epsilon_{\mathrm{M}}(\lambda, T^*) &= \lambda\epsilon_{\mathrm{Q}}(T^*) + (1 - \lambda)\epsilon_{\mathrm{H}}(T^*), \\ n_{\mathrm{BM}}(\lambda, T^*) &= \lambda n_{\mathrm{BQ}}(T^*) + (1 - \lambda)n_{\mathrm{BH}}(T^*), \end{aligned} \tag{7}$$

where $T^* = T^*(\mu)$ is the value of temperature on the phase boundary. which is determined by the Gibbs conditions of phase equilibrium. Figure 1 shows the entropy density as a function of temperature.

In a forthcoming publication, we will discuss the EoS dependence of physical observables utilizing a realistic lQCD-based equation of state, i.e., an EoS with a crossover phase transition at high T and low μ, including the QCD critical point [44]. We are currently in the process of constructing such an EoS, which will correctly capture critical phenomena

TABLE II. Mesons and meson resonances, sorted with respect to spin and parity, treated in the model.

0^-	1^-	0^+	1^+	2^+	$(1^-)^*$
π	ρ	a_0	a_1	a_2	$\rho(1450)$
K	K^*	K_0^*	K_1^*	K_2^*	$\rho(1700)$
η	ω	f_0	f_1	f_2	$\omega(1420)$
η'	ϕ	f_0^*	f_1'	f_2'	$\omega(1600)$

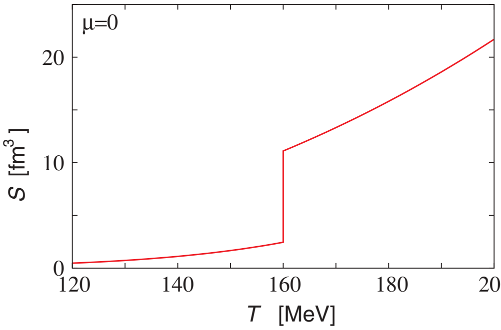

FIG. 1. (Color online) Entropy density as a function of temperature at $\mu = 0$. The critical temperature is 160 MeV.

around the QCD critical point [44]. A simple parametrization of the EoS around the QCD critical point as presented in [45] is unfortunately insufficient for a description of these phenomena, even though it already provides a marked improvement over currently used equations of state.

C. Initial conditions

The initial conditions for the hydrodynamic calculation need to be determined either by adjusting an appropriate parametrization to data or by utilizing other microscopic transport model predictions for the early nonequilibrium phase of the heavy-ion reaction.

Numerous studies exist for finding the appropriate initial conditions for hydrodynamic models [39,46–48]; usually such an initial condition is given by the parametrization of the spatial distribution of the energy or entropy density and baryon number density at an initial time τ_0. A comparison between final particle distributions calculated by the hydrodynamic model and experimental data can then be utilized to fix the values of the parameters for the initial conditions. However, this ansatz is problematic if no experimental data exist to tune the initial conditions. Furthermore, one loses predictive and analytic power by treating the quantities governing the initial conditions as free parameters. Recently, several attempts have been made to determine a set of initial conditions not from parametrizations and comparisons with data, but via a calculation using the color glass condensate (CGC) model for the initial state [17,47] as well as an approach combining perturbative QCD and the saturation picture [48]. A study of elliptic flow by Hirano *et al.* [17] has shown that additional dissipation during the early QGP stage is required if an initial condition based on the CGC is used. Another interesting fact found in hydrodynamic analyses at RHIC is that thermalization is achieved on very short time scales after the full overlap of the colliding nuclei: none of the hydrodynamic calculations which have successfully addressed RHIC data at the top energy of $\sqrt{s_{NN}} =$ 200 GeV/nucleon have initial times later than $\tau_0{\sim}0.6$ fm [14,49]. The physics processes leading to such a rapid thermalization have yet to be unambiguously identified [50]; note that hydrodynamics itself cannot address the question of thermalization, since it relies on the assumption of matter being in local thermal equilibrium.

For our calculation, we use a simple initial condition which is parametrized based on a combination of wounded nucleon and binary collision scaling [46,51,52]. Similar parametrizations used in various hydrodynamic models have been successful in explaining numerous experimental observations at RHIC [14,16,49]. We have chosen this common initial condition for our investigation in order to describe the general features of our model and provide a baseline comparison with previous calculations under similar assumptions. In a subsequent publication, we shall investigate the sensitivity of our results to particular variations and assumptions regarding the choice of the initial conditions.

We factorize the energy density and baryon number density distributions into longitudinal direction $H(\eta)$ and the transverse plane $W(x, y; b)$, which are given by

$$\begin{aligned} \epsilon(x, y, \eta) &= \epsilon_{\max} W(x, y; b) H(\eta), \\ n_B(x, y, \eta) &= n_{B\max} W(x, y; b) H(\eta), \end{aligned} \tag{8}$$

where $\epsilon_{\max}$ and $n_{B\max}$ are parameters which are maximum values of energy density and baryon number density. The longitudinal distribution is parametrized by

$$H(\eta) = \exp\left[-(|\eta| - \eta_0)/2\sigma_\eta^2\right]\theta(|\eta| - \eta_0), \tag{9}$$

where parameters η_0 and σ_η are determined by comparison with experimental data of single particle distributions. The function $W(x, y; b)$ on the transverse plane is determined by the superposition of wounded nucleon scaling, which is characteristic of "soft" particle production processes, and binary collision scaling, which is characteristic of "hard" particle production processes [53]. This function is normalized by $W(0, 0; 0)$. In the wounded nucleon scaling, the density of wounded nucleons is given by

$$\begin{aligned} \frac{d^2 N_{\mathrm{WN}}}{ds^2} = {} & T_A(\boldsymbol{b}_A) \cdot (1 - e^{-T_B(\boldsymbol{b}_B)\sigma}) \\ & + T_B(\boldsymbol{b}_B) \cdot (1 - e^{-T_A(\boldsymbol{b}_A)\sigma}), \end{aligned} \tag{10}$$

where $\boldsymbol{b}_A = \boldsymbol{s} + b \cdot e_x$ ($\boldsymbol{b}_B = \boldsymbol{s} - b \cdot e_x$), σ is the total nucleon-nucleon cross section at Au+Au $\sqrt{s_{NN}} = 200A$ GeV and set to 42 mb [54]. T_A is the nuclear thickness function of nucleus A,

$$T_A(s) = \int dz \rho_A(z, s), \tag{11}$$

where $\rho_A(z, \mathbf{s})$ is given by a Woods-Saxon parametrization of nuclear density,

$$\rho_A(r) = \rho_0 \frac{1}{1 + e^{(r - R_A)/a}}. \tag{12}$$

In Eq. (12), parameters a, R_A, and ρ_0 are 0.54 fm, 6.38, and 0.1688, respectively [54]. On the other hand, the distribution of the number of binary collisions is given by

$$\frac{d^2 N_{\mathrm{BC}}}{ds^2} = \sigma \cdot T_A(\boldsymbol{b}_A) T_B(\boldsymbol{b}_B). \tag{13}$$

Then total $W(x, y; b) = w \frac{d^2 N_{\mathrm{BC}}}{ds^2} + (1 - w) \frac{d^2 N_{\mathrm{WN}}}{ds^2}$, where w is the weight factor for binary scaling and is set to 0.6, again utilizing a comparison of experimental data of single particle spectra to our model calculations. Figures 2 and 3 show

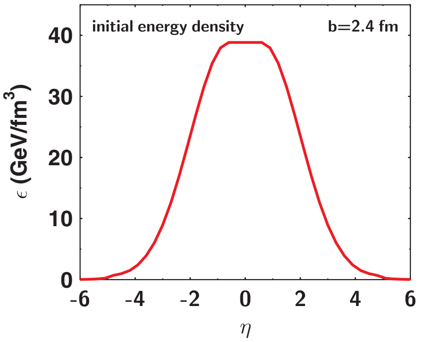

FIG. 2. (Color online) Initial energy density in longitudinal direction at Au+Au $\sqrt{s_{NN}} = 200$ GeV central collisions ($b = 2.4$ fm) in the case of hydro+UrQMD.

initial energy density in the longitudinal direction and on the transverse plane for Au+Au $\sqrt{s_{NN}} = 200$ GeV central collisions for the case of a hybrid hydro+micro calculation.

As a starting point, we set initial longitudinal flow to Bjorken's scaling solution [9] and neglect initial transverse flow. This is the simplest initial flow profile which will serve as the basis for further investigation. For example, Kolb and Rapp [55] discussed the possibility of the existence of an initial transverse flow which improves the results for P_T spectra and reduces the anisotropy in flow, but at the expense of introducing an additional parameter. Utilizing a parametrized evolution model, it has been pointed out that a Landau-type initial longitudinal compression and reexpansion of matter is favorable for the description of the Hanbury-Brown–Twiss (HBT) correlation radii [56]. This suggests that HBT analyses may be a sensitive tool for the determination of the initial longitudinal flow distribution.

Table III lists parameters with which we reproduce single particle spectra at RHIC. The parameters η_0 and σ_η in longitudinal direction are determined mainly by the hadron rapidity distributions and do not strongly affect the transverse momentum distributions. The parameters for the initial conditions need to be optimized separately for the pure hydro and hydro + UrQMD calculations. A comparison between the two sets of initial conditions and possible physics implications can be found in Sec. III. Comparing the initial energy density of our purely hydrodynamic calculation with that in Ref. [55], in which an initial condition was parametrized in terms of the entropy and baryon number density (weighted according to the wounded nuclear model by 75% and to the binary collision model by 25%), we find that our calculation requires a significantly higher initial energy or entropy density: the maximum value of the entropy density at Au + Au $\sqrt{s_{NN}} = 200$ GeV in central collision in [55] is 110 fm^{-3}, whereas our value of the maximum entropy density is 176 fm^{-3}. The difference between the two values is most likely due to the treatment of resonance decays—these are explicitly treated in [55], but are neglected in our case. Note that we consider our purely hydrodynamic calculation solely as a baseline against which we can compare the full hydro+micro model, which of course contains a proper treatment of resonance decays. A third hydrodynamic model implementation described in [47] uses an initial condition purely based on binary collisions. The maximum value of energy density in that calculation (which also treats resonance decays) is found to be ~45 GeV/fm^3, similar to the value we obtain for our hydro+micro calculation.

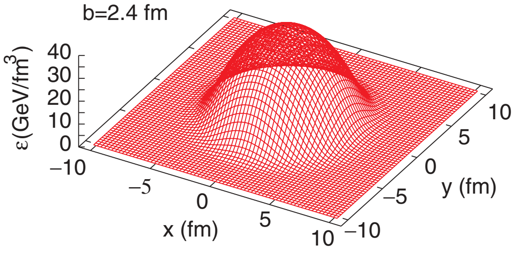

FIG. 3. (Color online) Same as Fig. 2, but for the transverse plane.

TABLE III. Parameters for initial conditions of pure hydro and hybrid model.

Model	τ_0 (fm/c)	$\epsilon_{\max}$ (GeV/fm^3)	$n_{B\max}$ (fm^{-3})	η_0	σ_η
Pure hydro	0.6	55	0.15	0.5	1.5
Hydro + UrQMD	0.6	40	0.15	0.5	1.5

D. Hadronization and the transition to microscopic dynamics

Having specified the initial conditions on the $\tau = \tau_i$ hypersurface and the EoS, we determine uniquely the hydrodynamic solution in the forward light cone. We assume that a freeze-out process happens when a temperature in a volume element of fluid is equal to a freeze-out temperature T_f in the pure 3D hydrodynamic model. In a hybrid model, the transition from macroscopic to microscopic dynamics takes place at a switching temperature $T_{\rm SW}$. The freeze-out and switching temperatures can be treated as parameters and determined by comparison with experimental data on single particle spectra.

Due to our use of Lagrangian hydrodynamics, grid points move along the flux of the fluid and are no longer represented by a fixed coordinate-space lattice. Therefore, it is nontrivial to estimate the number of particles flowing through the freeze-out hypersurface. Here we start from a simple case [57]: suppose that the number of particles $N(\tau)$ exists in the enclosed volume Ω that is bounded by a closed surface $S(\tau)$ at time τ. $N(\tau)$ is given by

$$N(\tau) = \int_{\Omega(\tau)} d^3 r n(\boldsymbol{r}, \tau), \tag{14}$$

where $n(\boldsymbol{r}, \tau)$ is particle number density. At time $\tau + \delta\tau$, the number of particle $N(\tau)$ changes to

$$\frac{dN}{d\tau} = \int_{\Omega(\tau)} d^3 r \frac{\partial n}{\partial \tau} + \frac{1}{d\tau} \int_{\delta\Omega} d^3 r n(\boldsymbol{r}, \tau), \tag{15}$$

where the volume varies to $\Omega + \delta\Omega$. Utilizing current conservation, $\frac{\partial n}{\partial \tau} + \nabla \cdot \boldsymbol{j}(\boldsymbol{j}$ is a current of particle), Eq.(15) is rewritten as

$$\frac{dN}{d\tau} = -\int_{S(\tau)} d^2s\, \boldsymbol{j}\cdot\boldsymbol{n} + \int_{S(\tau)} d^2s \frac{d\zeta}{d\tau} n, \tag{16}$$

where $\boldsymbol{n}$ is the normal vector of surface element d^2s, and $d\zeta$ is the distance between the surface of $\Omega(\tau)$ and that of $\Omega(\tau)+\delta\Omega$. In Eq. (16), $dN/d\tau$ is the number of particles which cross the surface $S(\tau)$ during $d\tau$. Then the total number of particles through the hypersurface Σ, which is the set of surfaces $\{S(\tau)\}$, is

$$N = \int_{\Sigma} j^{\mu} d\sigma_{\mu}, \tag{17}$$

where $j^0 = n, d\sigma_0 = d^3r, d\boldsymbol{\sigma} = d\tau \cdot d^2s\mathbf{n}$. If we write

$$j^{\mu} = \frac{d^3P}{E}\frac{g_h}{(2\pi)^3}\frac{1}{\exp[(P_{\nu}u^{\nu}-\mu_f)/T_f]\pm 1}P^{\mu} \tag{18}$$

for the current j^{μ} in Eq. (17), we obtain the Cooper-Frye formula [58]

$$E\frac{dN}{d^3P} = \sum_h \frac{g_h}{(2\pi)^3}\int_{\Sigma} d\sigma_{\mu}P^{\mu} \times \frac{1}{\exp[(P_{\nu}u^{\nu}-\mu_f)/T_f]\pm 1}, \tag{19}$$

where g_h is a degeneracy factor of hadrons, and T_f and μ_f are the freeze-out temperature and chemical potential. In other words, we obtain $d\sigma_{\mu}$ by estimating the normal vector on the freeze-out hypersurface Σ. Using Eq. (19), we then can calculate all particle distributions.

To pass on the distribution (19) in the macroscopic model to the microscopic model, we first calculate the multiplicities N_i for each particle species i by integrating Eq. (19) in which T_f and μ_f are changed to the switching temperature $T_{\rm SW}$ and chemical potential $\mu_{\rm SW}$ over space-time $(\tau, \boldsymbol{r}, \eta)$ and momentum space $(\boldsymbol{P}_T, y)$. N_i is rounded to an integer value since the hadronic transport model described in the next section deals with real particle degrees of freedom. The distribution (19) divided by N_i is used as a probability distribution to randomly generate the space-time and momentum-space coordinates for N_i hadrons of species i. This distribution serves as an input for the hadronic transport model for a single event. The sampling procedure can be repeated to generate a sequence of events as starting points for the microscopic calculation. Each event sampling produces a different set of space-time and momentum coordinates as input of the microscopic model; however, the total multiplicity for each species i remains constant for a given hydrodynamic switching hyper-surface. In a more realistic calculation, particle number fluctuations should be taken into account as well. The reverse process, absorbing microscopic particles into the hydrodynamic medium, is being neglected; it has been shown in [16] that for rapidly expanding systems, these contributions are negligible.

E. Microscopic dynamics: UrQMD approach

The ensemble of hadrons generated accordingly is then used as an initial condition for the microscopic transport model UrQMD [18]. The UrQMD approach is closely related to hadronic cascade [59], Vlasov-Uehling-Uhlenbeck [60], and (R)QMD transport models [61]. We shall describe here only the part of the model that is important for the application at hand, namely, the evolution of an expanding hadron gas in local equilibrium at a temperature of about $T_C \sim 160$ MeV. The treatment of high-energy hadron-hadron scatterings, as it occurs in the initial stage of ultrarelativistic collisions, is not discussed here. A complete description of the model and detailed comparisons with experimental data can be found in [18].

The basic degrees of freedom are hadrons modeled as Gaussian wave packets and strings, which are used to model the fragmentation of high-mass hadronic states via the Lund scheme [62]. The system evolves as a sequence of binary collisions or $(2-N)$-body decays of mesons, baryons, and strings.

The real part of the nucleon optical potential, i.e., a mean field, can in principle be included in UrQMD for the dynamics of baryons (using a Skyrme-type interaction with a hard equation of state). However, currently no mean field for mesons (the most abundant hadrons in our investigation) are implemented. Therefore, we have not accounted for mean fields in the equation of motion of the hadrons. To remain consistent, mean fields were also not taken into account in the EoS on the fluid-dynamic side. Otherwise, pressure equality (at given energy and baryon density) would be destroyed. We do not expect the effects of mean fields to cause large modifications of the results presented here, because the "fluid" is not very dense after hadronization. Moreover, current experiments at the GSI Schwerionen Synchrotron (SIS) and BNL Alternating Gradient Synchrotron (AGS) only point to strong medium-dependent properties of mesons (kaons in particular) for relatively low incident beam energies ($E_{\rm lab}\leqslant 4$ GeV/nucleon) [63]. Nevertheless, mean fields will have to be included in the future.

Binary collisions are performed in a point-particle sense: Two particles collide if their minimum distance d, i.e., the minimum relative distance of the centroids of the Gaussians during their motion, in their c.m. frame fulfills the requirement

$$d \leqslant d_0 = \sqrt{\frac{\sigma_{\rm tot}}{\pi}}, \qquad \sigma_{\rm tot} = \sigma(\sqrt{s},\ \text{type}). \tag{20}$$

The cross section is assumed to be the free cross section of the regarded collision type (N-N, N-Δ, π-N, ...).

The UrQMD collision term contains 53 different baryon species (including nucleon, δ, and hyperon resonances with masses up to 2 GeV) and 24 different meson species (including strange meson resonances), which are supplemented by their corresponding antiparticle and all isospin-projected states. The baryons and baryon resonances which can be populated in UrQMD are listed in Table I, the respective mesons in Table II; full baryon/antibaryon symmetry is included (though not shown in the table), with respect to both the included hadronic states and the reaction cross sections. All hadronic states can be produced in string decays, s-channel collisions, or resonance decays.

Tabulated and parametrized experimental cross sections are used when available. Resonance absorption, decays and scattering are handled via the principle of detailed balance. If no experimental information is available, the cross section is calculated either via a one-boson-exchange (OBE) model or via a modified additive quark model which takes basic phase-space properties into account.

In the baryon-baryon sector, the total and elastic proton-proton and proton-neutron cross sections are well known [64]. Since their functional dependence on $\sqrt{s_{NN}}$ shows a complicated shape at low energies, UrQMD uses a table lookup for those cross sections. However, many cross sections involving strange baryons and/or resonances are not well known or even experimentally accessible; for these cross sections, the additive quark model is widely used.

As we shall see later, the most important reaction channels in our investigation are meson-meson and meson-baryon elastic scattering and resonance formation. For example, the total meson-baryon cross section for nonstrange particles is given by

$$\sigma_{\text{tot}}^{\text{MB}}(\sqrt{s}) = \sum_{R=\Delta,N^*} \langle j_B, m_B, j_M, m_M \| J_R, M_R\rangle \times \frac{2S_R+1}{(2S_B+1)(2S_M+1)} \times \frac{\pi}{p^2_{\text{c.m.s.}}} \frac{\Gamma_{R\to\text{MB}}\Gamma_{\text{tot}}}{(M_R-\sqrt{s})^2+\frac{\Gamma^2_{\text{tot}}}{4}}, \tag{21}$$

with the total and partial $\sqrt{s}$-dependent decay widths Γ_{tot} and $\Gamma_{R\to\text{MB}}$. The full decay width $\Gamma_{\text{tot}}(M)$ of a resonance is defined as the sum of all partial decay widths and depends on the mass of the excited resonance:

$$\Gamma_{\text{tot}}(M) = \sum_{\text{br}=\{i,j\}}^{N_{\text{br}}} \Gamma_{i,j}(M). \tag{22}$$

The partial decay widths $\Gamma_{i,j}(M)$ for the decay into the final state with particles i and j is given by

$$\Gamma_{i,j}(M) = \Gamma_R^{i,j}\frac{M_R}{M}\left(\frac{\langle p_{i,j}(M)\rangle}{\langle p_{i,j}(M_R)\rangle}\right)^{2l+1} \times \frac{1.2}{1+0.2\left(\frac{\langle p_{i,j}(M)\rangle}{\langle p_{i,j}(M_R)\rangle}\right)^{2l}}, \tag{23}$$

where M_R denotes the pole mass of the resonance, $\Gamma_R^{i,j}$ its partial decay width into the channel i and j at the pole, and l the decay angular momentum of the final state. All pole masses and partial decay widths at the pole are taken from the Review of Particle Properties [64]. $\Gamma_{i,j}(M)$ is constructed in such a way that $\Gamma_{i,j}(M_R) = \Gamma_R^{i,j}$ is fulfilled at the pole. In many cases, only crude estimates for $\Gamma_R^{i,j}$ are given in [64]; the partial decay widths must then be fixed by studying exclusive particle production in elementary proton-proton and pion-proton reactions. Therefore, e.g., the total pion-nucleon cross section depends on the pole masses, widths, and branching ratios of all N^* and Δ^* resonances listed in Table I. Resonant meson-meson scattering (e.g., $\pi+\pi\to\rho$ or $\pi+K\to K^*$) is treated in the same formalism.

To correctly treat equilibrated matter [43] (we repeat that the hadronic matter with which UrQMD is being initialized in our approach is in local chemical and thermal equilibrium), the principle of detailed balance is of great importance. Detailed balance is based on time-reversal invariance of the matrix element of the reaction. It is most commonly found in textbooks in the form

$$\sigma_{f\to i} = \frac{\vec{p}_i^{\,2}}{\vec{p}_f^{\,2}}\frac{g_i}{g_f}\sigma_{i\to f}, \tag{24}$$

with g denoting the spin-isospin degeneracy factors. UrQMD applies the general principle of detailed balance to the following two process classes:

(i) Resonant meson-meson and meson-baryon interactions: Each resonance created via a meson-baryon or a meson-meson annihilation may again decay into the two hadron species which originally formed it. This symmetry is only violated in the case of three- or four-body decays and string fragmentations, since N-body collisions with ($N>2$) are not implemented in UrQMD.

(ii) Resonance-nucleon or resonance-resonance interactions: the excitation of baryon resonances in UrQMD is handled via parametrized cross sections which have been fitted to data. The reverse reactions usually have not been measured; here, the principle of detailed balance is applied. Inelastic baryon-resonance deexcitation is the only method in UrQMD to absorb mesons (which are *bound* in the resonance). Therefore, the application of the detailed balance principle is of crucial importance to heavy nucleus-nucleus collisions.

Equation (24), however, is only valid in the case of stable particles with well-defined masses. Since in UrQMD detailed balance is applied to reactions involving resonances with finite lifetimes and broad mass distributions, Eq. (24) has to be modified accordingly. For the case of one incoming resonance, the respective modified detailed balance relation has been derived in [65]. Here, we generalize this expression for up to two resonances in both the incoming and outgoing channels.

The differential cross section for the reaction $(1\,,\,2)\to(3\,,\,4)$ is given by

$$d\sigma_{12}^{34} = \frac{|\mathcal{M}|^2}{64\pi^2 s}\frac{p_{34}}{p_{12}}d\Omega\prod_{i=3}^{4}\delta\left(p_i^2-M_i^2\right)dp_i^2, \tag{25}$$

where the p_i in the δ function denote four-momenta. The δ function ensures that the particles are on-mass-shell, i.e., their masses are well defined. If the particle, however, has a broad mass distribution, then the δ function must be substituted by the respective mass distribution (including an integration over the mass), that is,

$$d\sigma_{12}^{34} = \frac{|\mathcal{M}|^2}{64\pi^2 s}\frac{1}{p_{12}}d\Omega\prod_{i=3}^{4}p_{34}\cdot\frac{\Gamma}{(m-M_i)^2+\Gamma^2/4}\frac{dm}{2\pi}. \tag{26}$$

Incorporating these modifications into Eq. (24) and neglecting a possible mass dependence of the matrix element, we obtain

$$\frac{d\sigma_{34}^{12}}{d\Omega} = \frac{\langle p_{12}^2 \rangle}{\langle p_{34}^2 \rangle} \frac{(2S_1+1)(2S_1+1)}{(2S_3+1)(2S_4+1)} \times \sum_{J=J_-}^{J_+} \langle j_1 m_1 j_2 m_2 \| J M \rangle \frac{d\sigma_{12}^{34}}{d\Omega}. \tag{27}$$

Here, S_i indicates the spin of particle i, and the summation of the Clebsch-Gordan coefficients is over the isospin of only the outgoing channel. For the incoming channel, isospin is treated explicitly. The summation limits are given by

$$J_- = \max(|j_1 - j_2|, |j_3 - j_4|), \tag{28}$$

$$J_+ = \min(j_1 + j_2, j_3 + j_4). \tag{29}$$

The integration over the mass distributions of the resonances in Eq. (27) has been denoted by the brackets $\langle\,\rangle$, e.g.,

$$p_{3,4}^2 \Rightarrow \langle p_{3,4}^2 \rangle = \int\int p_{\text{c.m.s.}}^2(\sqrt{s}, m_3, m_4) A_3(m_3) A_4(m_4) dm_3\, dm_4,$$

with the mass distribution $A_r(m)$ given by a free Breit-Wigner distribution with a mass-dependent width according to Eq. (22) as

$$A_r(m) = \frac{1}{N} \frac{\Gamma(m)}{(m_r - m)^2 + \Gamma(m)^2/4}, \tag{30}$$

with

$$\lim_{\Gamma \to 0} A_r(m) = \delta(m_r - m),$$

and the normalization constant

$$N = \int_{-\infty}^{\infty} \frac{\Gamma(m)}{(m_r - m)^2 + \Gamma(m)^2/4} dm. \tag{31}$$

Alternatively, one can also choose a Breit-Wigner distribution with a fixed width; the normalization constant then has the value $N = 2\pi$.

The most frequent applications of Eq. (27) in UrQMD are the processes $\Delta_{1232} N \to NN$ and $\Delta_{1232}\Delta_{1232} \to NN$.

III. RESULTS

A. Modeling of the entire reaction dynamics in three-dimensional hydrodynamics

The purpose of this section is to establish a baseline against which we can later compare the results of our hybrid macro+micro model. In addition, we wish to demonstrate that our novel implementation of the $3+1$ dimensional relativistic hydrodynamic model, utilizing a Lagrangian grid, is capable of reproducing the results of previous hydrodynamic calculations. Many of these previous calculations found in the literature have focused on one or two particular observables; here, we wish to conduct a consistent analysis of all relevant single particle distributions which can be addressed by a hydrodynamic calculation.

To obtain qualitative results which are comparable to experimental data, we have to determine the parameters of the initial conditions. This is accomplished by adjusting the parameters to fit the single particle spectra for the most central Au+Au collisions at $\sqrt{s_{NN}} = 200$ GeV.

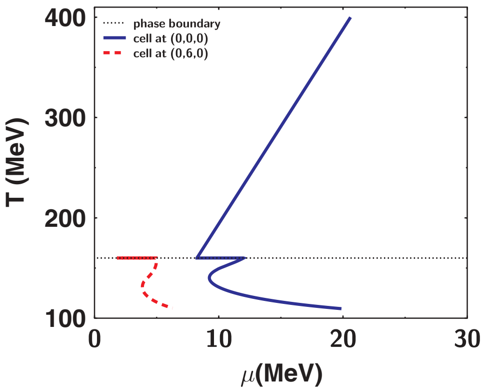

FIG. 4. (Color online) Isentropic trajectories on T-μplane. Solid (dashed) line stands for the behavior of cell located at $(x, y, \eta) = (0, 0, 0)[= (0, 6, 0)]$ at initial time. Dotted line represents phase boundary.

First we show the behavior of isentropic trajectories in the T-μ plane for Au+Au $\sqrt{s_{NN}} = 200$ GeV central collisions in Fig. 4. The dotted line stands for the phase boundary between the QGP and the hadronic phase. (Note that due to small baryochemical potentials, the phase boundary is an almost flat line at $T_C = 160$ MeV.) Apart from the central cell, we also investigate the isentropic trajectory of a cell close to the surface of the initially produced QGP. Whereas the isentropic trajectory of the central cell located at (0,0,0) starts in the QGP phase (solid line), the cell at the initial surface of the QGP (dashed line) only exhibits an evolution from the mixed phase to the hadronic phase. Both trajectories are terminated at freeze-out temperature, $T_{\mathrm{f}} = 110$ MeV.

Figure 5 shows the P_T spectra of π, K and p in Au+Au at $\sqrt{s_{NN}} = 200$ GeV for central collisions. Our calculation

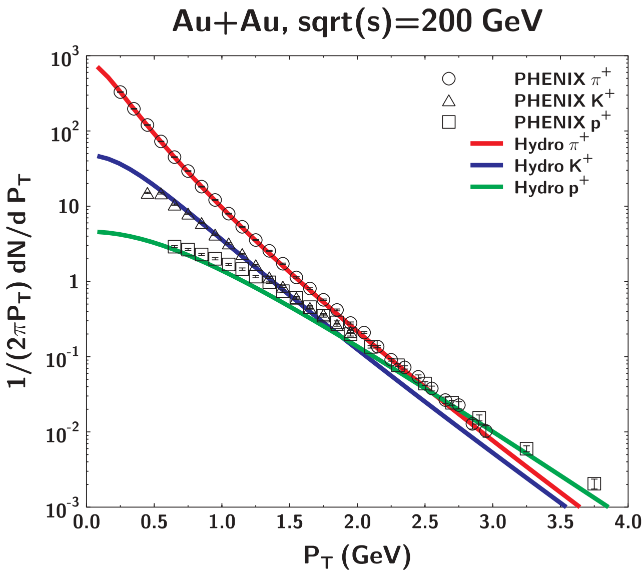

FIG. 5. (Color online) P_T spectra for π^+, K^+, p at central collisions with PHENIX data [66]. For proton, we rescale our result using the ratio at chemical temperature (see text).

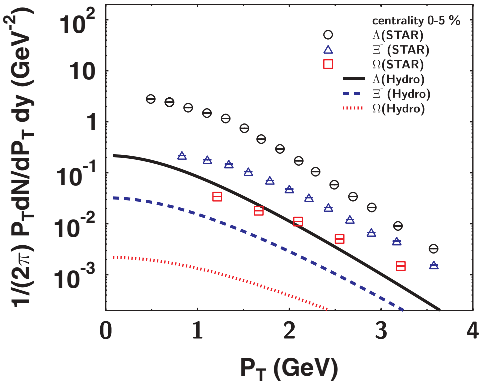

FIG. 6. (Color online) P_T spectra for multistrange baryons at central collisions with STAR data [67]. In this calculation (pure hydro), normalization is not done.

succeeds in reproducing the π spectra measured by the PHENIX collaboration [66] up to $P_T \sim 2$ GeV. However, because of the model assumption of chemical equilibrium up to the (low) kinetic freeze-out temperature, we fail to obtain the correct normalization and hadron ratios, even though the shape of the P_T spectra of p and multistrange baryons (shown in Fig. 6) is close to experimental data. To obtain the proper normalization for the p spectra and match the experimentally measured hadron ratios, we adopt a procedure outlined in Ref. [68], which renormalizes the P_T spectra using the p to π ratio at the critical temperature to fix the normalization of the proton spectra. It is straightforward to extend this procedure to hyperons and multistrange baryons as well, even though we choose to show the real, unrenormalized result for the multistrange baryons in Fig. 6 to elucidate the situation prior to renormalization.

The need for renormalizing the p spectra suggests that the assumption of a continuous chemical equilibrium until kinetic freeze-out is not realistic and that an improved treatment of the freeze-out process is required. One method to deal with the separation of chemical and thermal freeze-out is the partial chemical equilibrium model (PCE) [14,55,69]: below a chemical freeze-out temperature $T_{\rm ch}$, one introduces a chemical potential for each hadron whose yield is supposed to be frozen out at that temperature. The PCE approach can account for the proper normalization of the spectra; however, it fails to reproduce the transverse momentum and mass dependence of the elliptic flow [70]. In Sec. III B, we shall utilize our hybrid hydro+micro model to decouple chemical and kinetic freeze-out. In these hybrid approaches [15–17], the freeze-out occurs sequentially as a result of the microscopic evolution, and flavor degrees of freedom are treated explicitly through the hadronic cross sections of the microscopic transport, leading to the proper normalization of all hadron spectra.

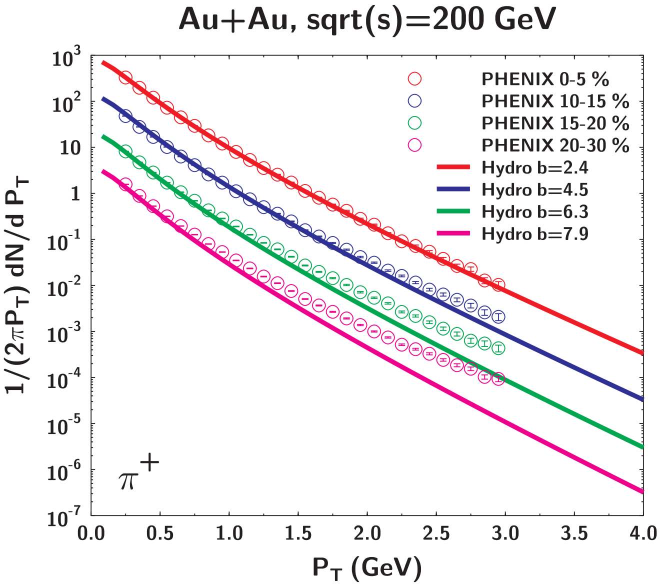

FIG. 7. (Color online) Centrality dependence of P_T spectra of π^+ with PHENIX data [66]. P_T spectra at 10–15%, 15–20%, and 20–30% are divided by 5, 25, and 200, respectively.

In Fig. 7, the centrality dependence of P_T spectra for π^+ is shown. The impact parameters are set to $b = 2.4, 4.5, 6.3, 7.9$ fm corresponding to 0–6%, 10–15%, 15–20%, 20–30% centrality, respectively. These values are estimated via the number of nucleon-nucleon binary collisions and the number of participant nucleons in Ref. [66]. The centrality dependence is determined simply by the collision geometry—no additional parameter is necessary for our finite impact parameter collision calculations in Sec. II C. Our results are consistent with the experimental data [66] in the low transverse momentum region ($0 < P_T < 1$ GeV) for all centralities. We observe that in peripheral collisions, the difference between experimental data and our calculations appears at lower P_T compared to central collisions. This difference is indicative of the diminished importance of the soft collective physics described by hydrodynamics compared with the contribution of jet physics in peripheral events.

Figure 8 shows the centrality dependence of the pseudorapidity distribution of charged hadrons compared with PHOBOS data [71]. The parameters of our initial condition in the longitudinal direction (σ_η, η_0) have been determined by fitting the data for the most central collisions; no additional parameter is needed to fix the initial conditions for noncentral collisions,

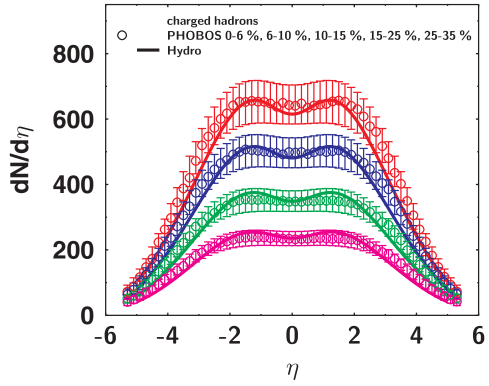

FIG. 8. (Color online) Centrality dependence of pseudorapidity distribution with PHOBOS data [71]. Impact parameters in the hydrodynamic model are 2.4, 4.5, 6.3, 7.5 fm from central to peripheral collisions.

since they result solely from the collision geometry. The impact parameters for our calculation are set to $b = 2.4, 4.5, 6.3$, and 7.9 fm corresponding to 0–6%, 6–15%, 15–25%, and 25%–35% centrality, respectively [71]. We find our results give good agreement with the experimental data not only at midrapidity but also at forward and backward rapidities, suggesting that the pure 3D hydrodynamic model can explain the charged hadron multiplicity distribution in a wide rapidity range. This observation is consistent with results of other pure hydrodynamic models [14,20,72] utilizing different computational methods. However, as we show later, the hydrodynamic calculation overestimates the elliptic flow at forward/backward rapidity, indicating that the rapidity distribution is rather insensitive to the details of the expansion dynamics. Having fixed all parameters of our initial condition utilizing the P_T spectra and (pseudo)rapidity distributions in the most central collisions, we now apply our hydrodynamic model to other physical observables using these parameters.

The elliptic flows as a function of P_T in 5–10% and 10–20% most central collisions are shown in Fig. 9 together with STAR data [73] at midrapidity. We set the impact parameter in our hydrodynamic calculation to 4.5 fm (6.3 fm) for the 5–10%(10–20%) data. In the case of the 5–10% most central events, we obtain reasonable agreement with the data for π and p. On the other hand, in the 10–20% centrality bin, our hydrodynamic calculation overpredicts the elliptic flow compared with experimental data. Especially for protons, the deviation between calculation and experimental data is fairly large; this trend has already been observed in [14].

Figure 10 shows the elliptic flow as a function of η in central (3–15%) and midcentral collisions (15–25%). In both cases, our hydrodynamic model calculations overestimate the elliptic flow at forward and backward rapidities, similar to results shown in Ref. [14]. At large forward and backward rapidities, the assumptions of a perfect hydrodynamic model such as local equilibrium, vanishing mean free path, and neglect of viscosity effect apparently are no longer valid. The deviations at forward and backward rapidities between experimental data and calculated results increase with the impact parameter, indicating a decrease of the volume in which hydrodynamic limit is achieved.

Summarizing this section, we have applied our ideal 3D RFD model to Au+Au collisions at the top RHIC energy. A set of parameters for the initial conditions has been determined which allows for the simultaneous description of π, K, and p P_T spectra, the charged hadron rapidity distribution, and the P_T as well as rapidity dependence of the elliptic flow coefficient v_2 for π and p. Without any additional parameters, the 3D RFD model is capable of describing the centrality dependence of the P_T spectra and the charged hadron rapidity distribution as well.

However, our analysis also has demonstrated a couple of deficits of the ideal 3D RFD approach, many of which are already well-known and have been discussed in the literature before [12,14]:

(i) The centrality dependence of the elliptic flow coefficient v_2 as a function of P_T is not well described.

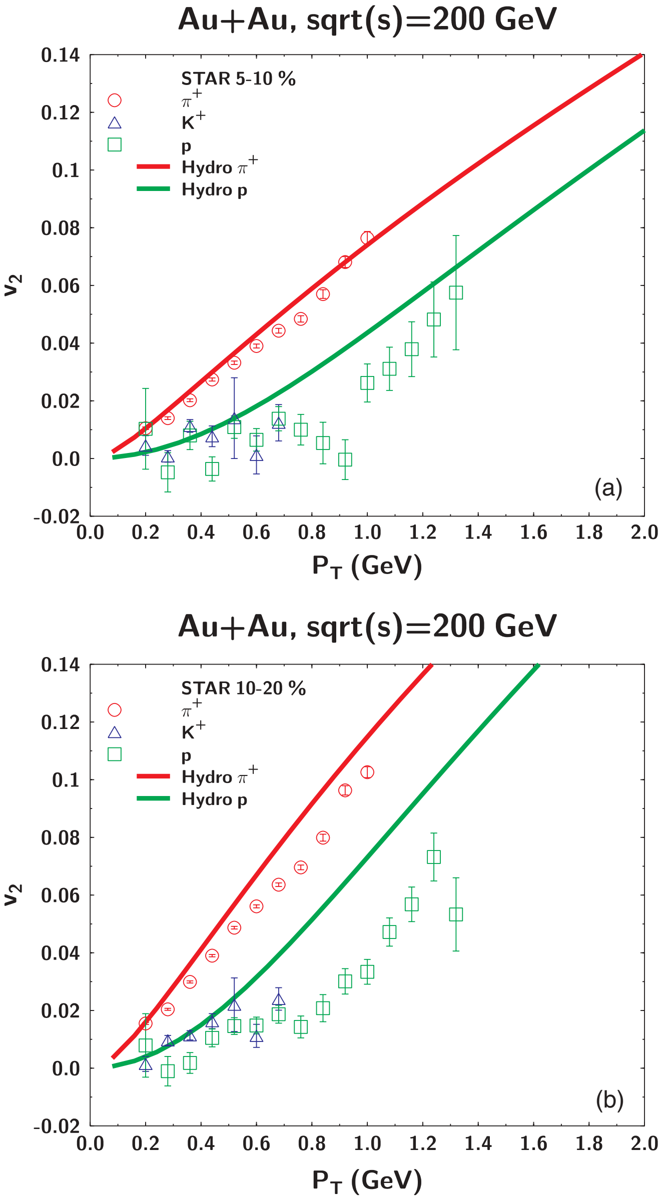

FIG. 9. (Color online) Elliptic flow as a function of P_T with STAR data [73] in centrality 5–10% (a) and in centrality 10–20% (b). Impact parameters in hydrodynamic calculations are 4.5 fm (a) and 6.3 fm (b).

(ii) The width of the v_2 vs η distribution is too broad compared with data.

(iii) p and multistrange particle spectra need to be normalized by hand in order to account for the separation of chemical and kinetic freeze-out.

(iv) The hydrodynamic approach is only of limited applicability for small systems (i.e., large impact parameters) and large P_T (hard physics).

In the following section, we shall use the 3D RFD calculation as a baseline to determine the effects of an improved treatment of the hadronic phase in the framework of the hydro+micro approach.

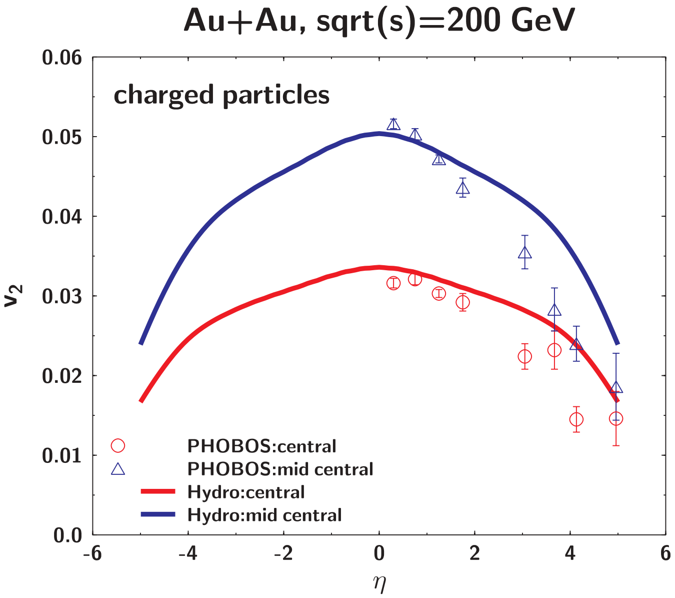

FIG. 10. (Color online) Elliptic flow as a function of η with PHOBOS experimental data [74] for central (3–15%) and midcentral collisions (15–25%). Impact parameters are set to 4.5 (central) and 6.3 (midcentral) fm, respectively.

B. Application of the hydro+micro approach

As in the previous subsection, we first determine the parameters of the initial conditions in Sec. II C by fitting the single particle spectra in the most central centrality bin. Table III shows the parameters for both the pure 3D RFD initial condition and the hydro+micro initial condition. The main difference we find between the two is in the maximum value of initial energy density. The large difference in the initial energy densities can be explained by our omission of resonance decays in the pure hydrodynamic calculation and to a lesser extent by the dissipative corrections present in the hydro+micro calculation. Both effects result in additional particle production, leading to smaller initial energy and entropy densities necessary to describe the final particle multiplicities.

We set the switching temperature T_{SW} to 150 MeV. This allows for a brief period of hydrodynamic evolution in the hadronic phase to account for multiparticle collisions which can occur at large densities and temperatures in the hadronic phase close to the phase boundary [75,76]. The dependence of hadronic observables on T_{SW}, such as the mean transverse momentum $\langle P_T \rangle$ of the different hadron species, has been investigated in [15]; our choice of 150 MeV conforms to the lower bound of the allowed range for T_{SW}.

Figure 11 shows the P_T spectra of π^+, K, and p at $\sqrt{s_{NN}} = 200$ GeV central collisions. The most compelling feature, compared with the pure 3D RFD calculation, is that the hydro+micro approach is capable of accounting for the proper normalization of the spectra for all hadron species without any additional correction as performed in the pure hydrodynamic model. The introduction of a realistic freeze-out process provides, therefore, a natural solution to the problem of separating chemical and kinetic freeze-out in a pure hydrodynamic approach. Similar results have been obtained previously in 1+1 and 2+1 dimensional implementations of the hydro+micro approach [15,16].

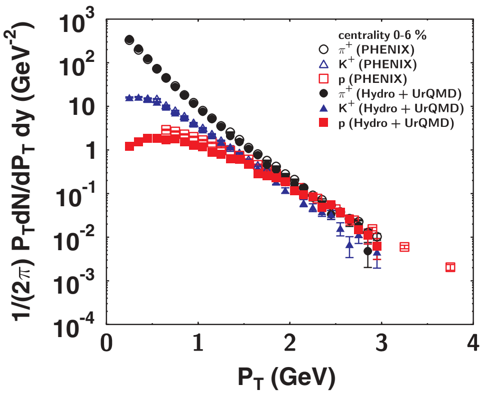

FIG. 11. (Color online) P_T spectra for π^+, K^+, and p at central collisions with PHENIX data [66]. The points are NOT renormalized.

In Fig. 12, centrality dependence of P_T spectra of π^+ is shown. The impact parameter for each centrality is determined in the same way as in the pure hydrodynamic calculation. The separation between model results and experiment appears at lower transverse momentum in peripheral collisions compared to central collisions, just as in the pure hydrodynamic calculation. The 3D hydro+micro model does not improve the results for this behavior, since the hard physics high-P_T contribution to the spectra occurs at early reaction times before the system has reached the QGP phase and is therefore included in neither the pure 3D RFD calculation nor the hydro+micro approach.

Figure 13 shows the centrality dependence of the pseudorapidity distribution of charged hadrons compared to PHOBOS data [71]. Solid circles stand for model results and open circles denote data taken by the PHOBOS Collaboration [71]. The impact parameters are set to $b = 2.4, 4.5, 6.3$, and 7.9 fm for 0–6%, 6–15%, 15–25%, and 25–35% centralities, respectively. Our results are consistent with experimental data over a wide pseudorapidity region. We observe a small deviation around $|\eta| \sim 3$, which may be improved by tuning the parameter σ_η (here we have chosen the same value as for the

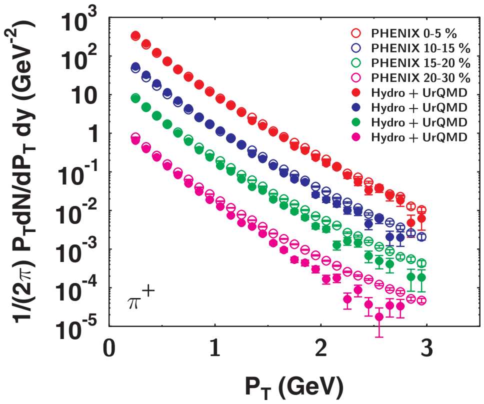

FIG. 12. (Color online) Centrality dependence of P_T spectra of π^+ with PHENIX data [66]. The P_T spectra at 10–15%, 15–20%, and 20–30% are divided by 5, 25, and 200, respectively.

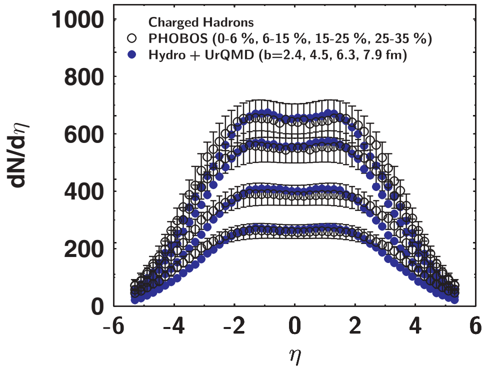

FIG. 13. (Color online) Centrality dependence of pseudorapidity distribution of charged particles with PHOBOS data [71]. Impact parameters in a calculation are 2.4 (0–6%), 4.5 (6–10%), 6.3 (10–15%), 7.5 fm (25–35%).

pure RFD calculation). There is no distinct difference between the 3D ideal RFD model and the hydro+UrQMD model in the centrality dependence of the pseudorapidity distribution, indicating that the shape of pseudorapidity distribution is insensitive to the detailed microscopic reaction dynamics of the hadronic final state.

In Fig. 14, we analyze the P_T spectra of multistrange particles. Our results show good agreement with experimental data for Λ, Ξ, Ω for centralities 0–5% and 10–20%. In this calculation, the additional procedure for normalization is not needed. Recent experimental results suggest that at thermal freeze-out, multistrange baryons exhibit less transverse flow and a higher temperature closer to the chemical freeze-out temperature compared to non- or single-strange baryons [67,77]. This behavior can be understood in terms of the flavor dependence of the hadronic cross section, which decreases with increasing strangeness content of the hadron. The reduced cross section of multistrange baryons leads to a decoupling from the hadronic medium at an earlier stage of the reaction, allowing them to provide information on the properties of the hadronizing QGP that is less distorted by hadronic final state interactions [16,78,79]. It should be noted that the analogous behavior has already been observed in experiments at the CERN SPS [80]. Later in this section, we will discuss the reaction dynamics of multistrange baryons in greater detail by analyzing the baryon collision number and freeze-out time distributions as well as their collision rates.

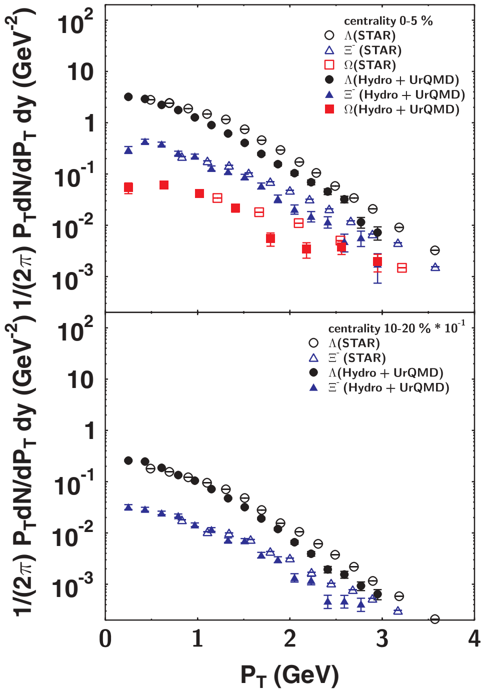

FIG. 14. (Color online) P_T spectra of multistrange particles at centralities 0–5% and 10–20% with STAR data [67].

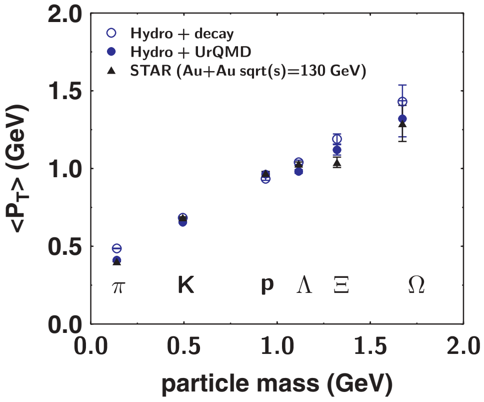

FIG. 15. (Color online) Mean P_T as a function of mass.

In Fig. 15, the mean transverse momentum $\langle P_T \rangle$ as a function of hadron mass is shown. Open symbols denote the value at $T_{\rm sw} = 150$ MeV, corrected for hadronic decays. Not surprisingly, in this case $\langle P_T \rangle$ follows a straight line, suggesting a hydrodynamic expansion. However, if hadronic rescattering is taken into account (solid circles), $\langle P_T \rangle$ does not follow the straight line: the $\langle P_T \rangle$ of pions is actually reduced by hadronic rescattering (they act as a heat bath in the collective expansion), whereas protons actually pick up additional transverse momentum in the hadronic phase. RHIC data by the STAR Collaboration is shown via the solid triangles: overall, the proper treatment of hadronic final state interactions significantly improves the agreement of the model calculation with the data. We should note that our results confirm those previously obtained in 1+1 and 2+1 dimensional implementations of the hydro+micro approach [15,16], demonstrating the robustness of the hydro+micro approach across three different implementations of the hydrodynamic and macro-to-micro transition components of the model.

Let us now investigate the effect of resonance decays and hadronic rescattering on the pion and baryon transverse momentum spectra: Figure 16 shows the P_T spectrum for π^+ at $T_{\rm sw} = 150$ MeV (solid line, uncorrected for resonance decays) as well as the final spectrum after hadronic rescattering and resonance decays, labeled Hydro+UrQMD (solid symbols). In addition, the open symbols denote a calculation with the resonance decay correction performed at $T_{\rm sw}$, which we labeled Hydro+decay. The difference between the solid line and open symbols, therefore, directly quantifies the effect of resonance

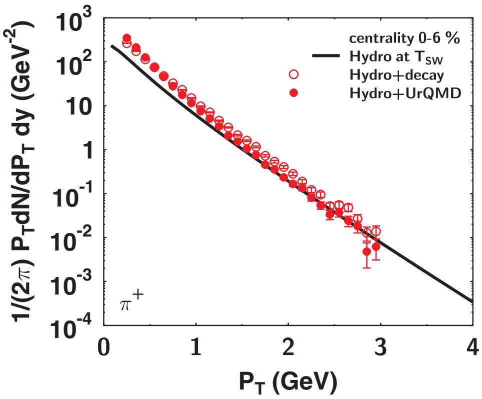

FIG. 16. (Color online) P_T spectra of π^+ from hydro at switching temperature, hydro+decay, and hydro+UrQMD at central collision.

decay on the spectrum, which is most dominant in the low transverse momentum region $P_T < 1$ GeV. Furthermore, the comparison between open and solid symbols quantifies the effect of hadronic rescattering: pions with $P_T > 1$ GeV lose momentum via these final state interactions, resulting in a steeper slope.

Figure 17 shows a likewise analysis for baryons (p, Λ, Ξ, and Ω). We note that in contrast to SPS energies [15], there is very little effect on the spectra due to hadronic rescattering, even for protons that rescatter 8–10 times at midrapidity. Only at low transverse momenta are the multiple scatterings of the protons (predominantly with pions) manifested in a slight flattening of the P_T distribution of the protons, giving rise to a slight increase in their radial flow. This phenomenon has been discussed in Ref. [15] and is commonly referred to as pion wind.

Figure 18 shows the distribution of the number of collisions that particles suffer in the hadronic phase at $b = 2.4$, 4.5, and 6.3 fm. The distributions for protons and Λ's are very broad, indicating a large amount of rescattering taking place in the hadronic phase. Around midrapidity, protons rescatter on average 10 times for central and semicentral impact parameters and Λ's rescatter 7–8 times (see also Fig. 19.). However, the average number of collisions of multistrange baryons is less than half those for protons and Λ's, as is to be expected because of the decrease of the hadronic cross section with increasing strangeness content of the hadron. We note that the collision number distributions change significantly as a function of centrality; for large impact parameters, the high-n_{coll} tail of the distribution exhibits a much steeper drop as a function of n_{coll}.

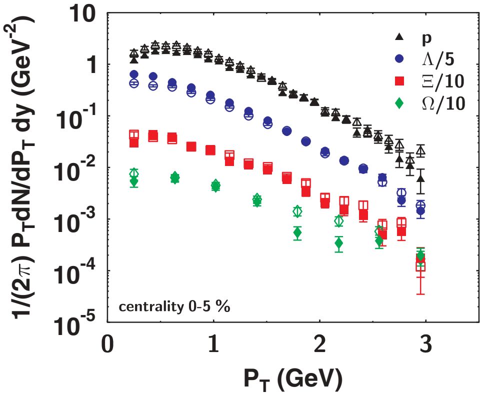

FIG. 17. (Color online) P_T spectra of baryons from hydro+decay (open symbols) and hydro+UrQMD (solid symbols) at centrality 0–5%.

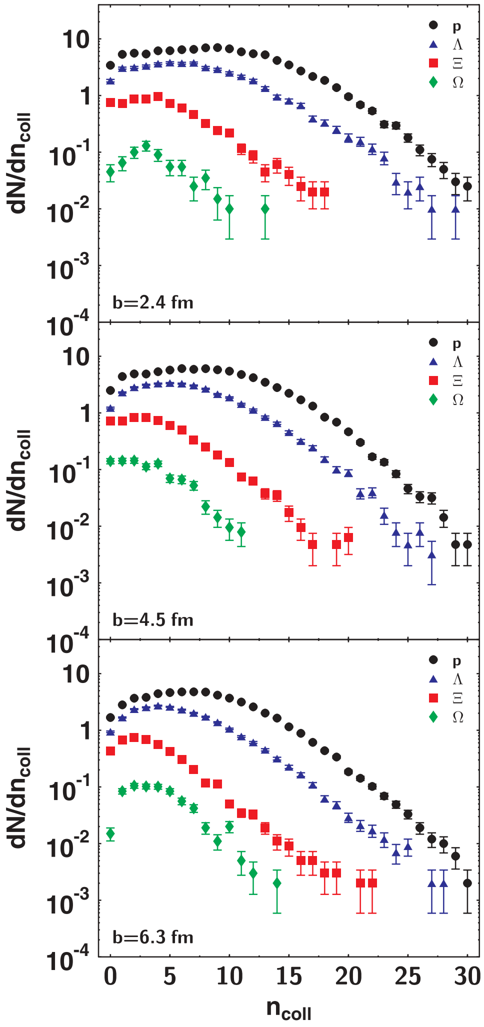

FIG. 18. (Color online) Impact parameter dependence of distribution of number of collisions for p, Λ, Ξ, Ω.

The pseudorapidity dependence of the number of hadronic rescatterings for different baryon species is analyzed in Fig. 19, which shows the number of collisions of p, Λ, Ξ and Ω as a function of η at $b = 2.4, 4.5$, and 6.3 fm. The distributions appear to be similar to that of the particle yield pseudorapidity distribution. At midrapidity, we find a plateau region extending from $\eta = -3$ to 3, followed by a steep drop-off to forward and backward rapidities. The flavor dependence of the average collision numbers is again clearly seen, even though we would like to point out that the shapes of the different distributions are very similar. The large plateau region indicates the rapidity domain in which *interacting* matter can be found and in which the application of thermodynamic concepts is viable.

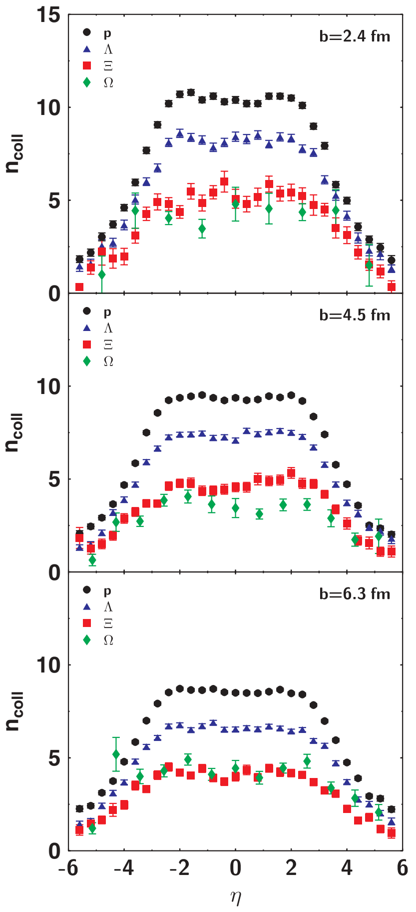

FIG. 19. (Color online) Same as Fig. 18, but as a function of η.

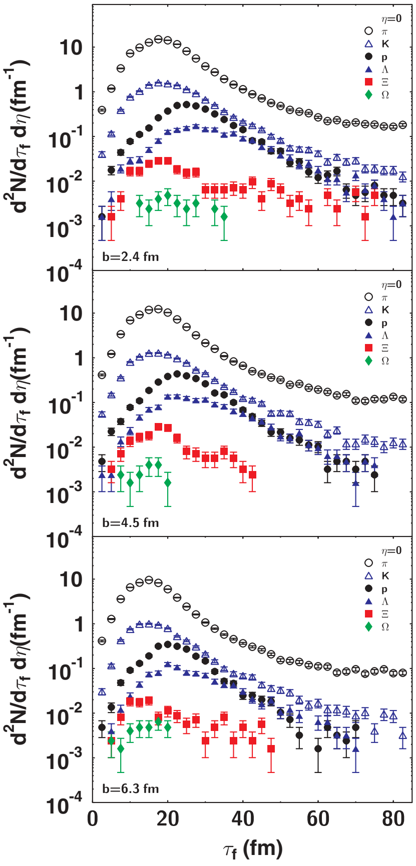

FIG. 20. (Color online) Freeze-out time distributions of π, K, p, Λ, Ξ, and Ω at midrapidity for $b = 2.4, 4.5, 6.3$ fm.

Figure 20 depicts the freeze-out time distributions of π, K, p, Λ, Ξ, and Ω at midrapidity for $b = 2.4, 4.5$, and 6.3 fm. The freeze-out time distributions of π and K peak around $\tau \sim 19$ (< 20 fm), while the peaks of the p and Λ freeze-out time distributions are shifted to later times. We also note that the freeze-out time of multistrange baryons is much smaller than that of other particles. The freeze-out times are in general determined by the amount of hadronic rescattering suffered by the different hadron species; our analysis indicates that (a) hadronic freeze-out is strongly species dependent and (b) even for a particular species, the freeze-out distribution is broad and it is therefore nearly impossible (or at least extremely ambiguous) to define a precise freeze-out time for a given hadron species.

This figure again supports the finding that multistrange baryons are produced with few interactions right after hadronization and freeze-out early [16,78,79], indications of which have been observed by the STAR Collaboration [67,77]. Given the broad freeze-out time distributions, it is very difficult to quantify the overall duration of the heavy-ion reaction; a possible criterion would be the drop-off of the number of freezing out particles per unit time and rapidity below 1, which would put the overall duration of the reaction to approximately 30 fm/c.

In Fig. 21, we study the effect hadronic rescattering has on the duration of the freeze-out process by comparing a calculation terminated at $T_{\rm sw}$ without hadronic rescattering (open symbols) to one including the full hadronic final state interactions (solid symbols). If we terminate at $T_{\rm sw}$, most hadrons freeze-out around 10 fm/c, reflecting the lifetime of the deconfined phase in our calculation (the tails of the distribution stem from the decays of long-lived resonances). The inclusion of hadronic rescattering shifts the peak of the freeze-out distribution to larger freeze-out times ($\tau_f \sim 20$–30),

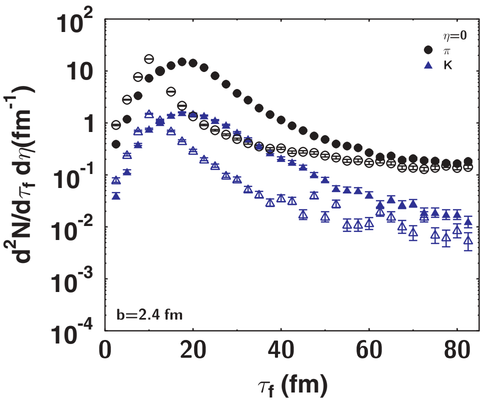

FIG. 21. (Color online) Freeze-out time distribution of mesons for hydro+decay (open symbols) and hydro+UrQMD (solid symbols) at midrapidity in the case of central collision.

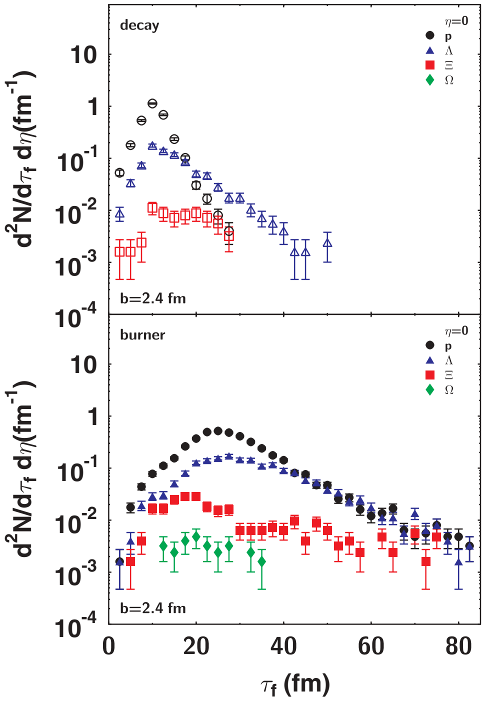

FIG. 22. (Color online) Freeze-out time distribution of baryons for hydro+decay (open symbols, above) and hydro+UrQMD (solid symbols, below) at midrapidity.

providing us with an estimate on the lifetime of the hadronic phase around 10–20 fm/c. Note that this estimate is subject to the same systematic uncertainties discussed previously in the context of the overall lifetime of the system.

The findings discussed in the context of the previous figure for pions and kaons are confirmed by analyzing baryons in the same fashion, which is shown in Fig. 22: here, the top frame contains the analysis terminated at T_{sw} and the bottom frame contains the calculation including full hadronic rescattering.

Figure 23 shows collision rates for meson-meson, meson-baryon, and baryon-baryon collisions at midrapidity and an impact parameter of $b = 2.4$ fm. We find that the reaction dynamics in the hadronic phase is dominated by meson-meson and to a lesser degree by meson-baryon interactions. Baryons essentially propagate in a medium dominated by mesons—a situation very different from the regime at AGS and lower SPS energies.

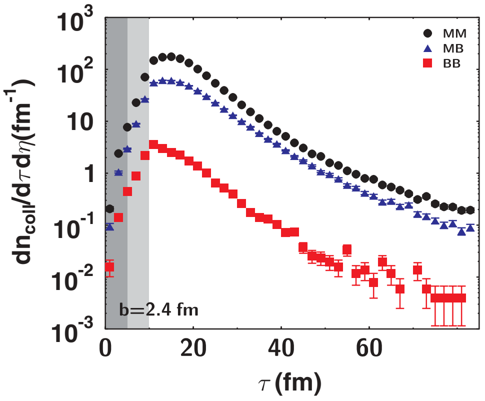

FIG. 23. (Color online) Collision rate for meson-meson (MM), meson-baryon (MB), and baryon-baryon (BB) at central collisions. The (dark) grey zone stands for QGP (mixed) phase, which is determined by the center cell.

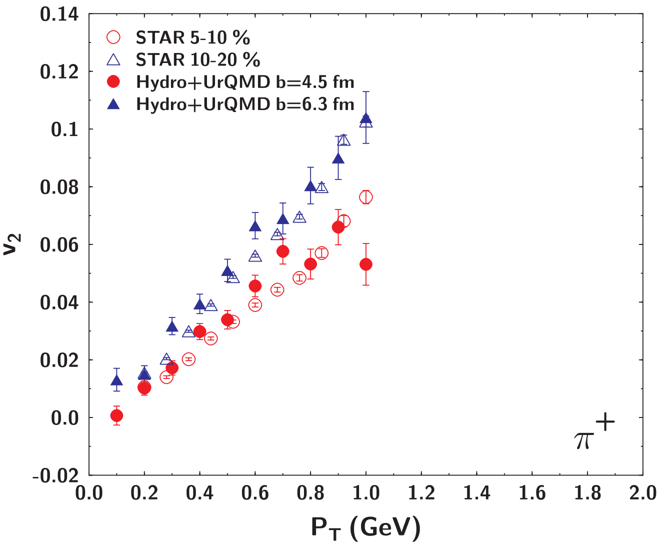

FIG. 24. (Color online) Elliptic flow as a function of P_T for π^+ at centralities 5–10% and 10–20%.

Finally, let us move to the analysis of elliptic flow in the hydro+micro approach. First we show the elliptic flow coefficient v_2 as a function of P_T for π^+ at centralities 5–10% and 10–20% in Fig. 24. Open symbols stand for experimental data and solid symbols represent our calculations. We find that the hydro+micro approach provides an improved agreement with the data compared to the purely hydrodynamic calculation (see Fig. 9 for comparison).

Figure 25 shows the elliptic flow coefficient v_2 as a function of pseudorapidity η for charged particles in central (3–15%) and midcentral (15–25%) collisions. The solid line stands for a purely hydrodynamic calculation (see Fig. 10), whereas the solid circles denote the hydro+micro approach and the solid triangles represent PHOBOS data [74]. We find that the dissipative effects contained in the hydro+micro approach significantly alter the shape of the v_2 vs η curve, providing a far better agreement with the data—in particular for pseudorapidities away from midrapidity. The analysis shows that apparently dissipative effects increase toward projectile and target rapidities, where the assumptions of ideal fluid dynamics break down earlier. Our analysis confirms the findings of [17], in which the effect of a color-glass initial condition on the elliptic flow rapidity dependence was also studied.

The question of how much elliptic flow develops during the deconfined phase vs the hadronic phase is investigated in Figs. 26 and 27. It has been pointed out repeatedly, both in the framework of microscopic [81] as well as as hydrodynamic analysis [52], that elliptic flow develops early on during the deconfined phase of the reaction and thus serves as a sensitive tool to the equation of state of QCD matter. This picture has been confirmed by the experimentally observed

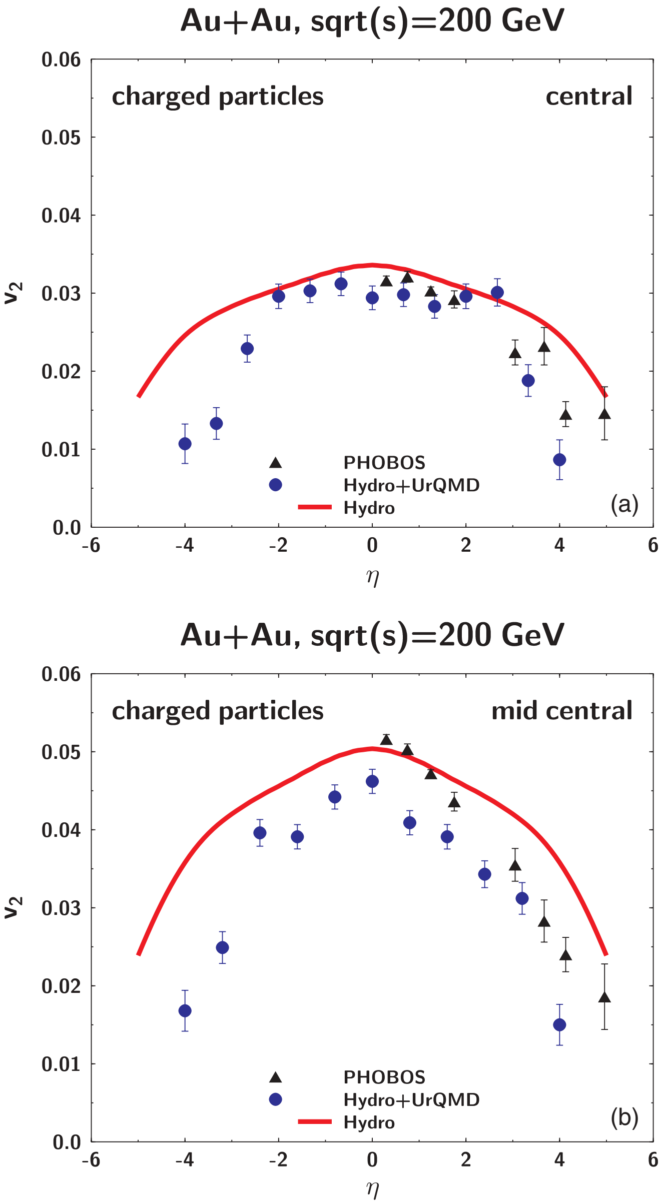

FIG. 25. (Color online) Elliptic flow as a function of η of charged particles at central and midcentral collisions. Impact parameters in the calculation are set to 4.5 fm (a) and 6.3 fm (b). PHOBOS data are from [74].

quark number scaling $v_2^h \sim n v_2(1/nP_T)$ of elliptic flow at intermediate transverse momenta P_T [82,83].

In Fig. 26, we plot elliptic flow v_2 as a function of P_T. The solid line stands for the pure hydro calculation, terminated at the switching temperature $T_{\rm sw}$, and solid circles denote the full hydro+micro calculation. We find that the QGP contribution to the elliptic flow depends on the transverse momentum: for low P_T, nearly 100% of the elliptic flow is created in the QGP phase of the reaction, whereas the hadronic phase contribution increases to 25% at a P_T of 1 GeV/c.

Figure 27 shows the elliptic flow as a function of η: the pure hydrodynamic calculation is shown by the solid curve, the hydrodynamic contribution at $T_{\rm sw}$ is denoted by the dashed line, and the full hydro+micro calculation is given by the solid circles, together with PHOBOS data (solid triangles). The shape of the elliptic flow in the pure hydrodynamic calculation at $T_{\rm sw}$ is quite different from that of the full hydrodynamic one terminated at a freeze-out temperature of 110 MeV. Apparently, the slight bump at forward and backward rapidities observed in the full hydrodynamic calculation develops first in the later hadronic phase, since it is not observed in the calculation terminated at $T_{\rm sw}$. Evolving the hadronic phase in the hydro+micro approach will increase the elliptic flow at central rapidities, but not in the projectile and target rapidity

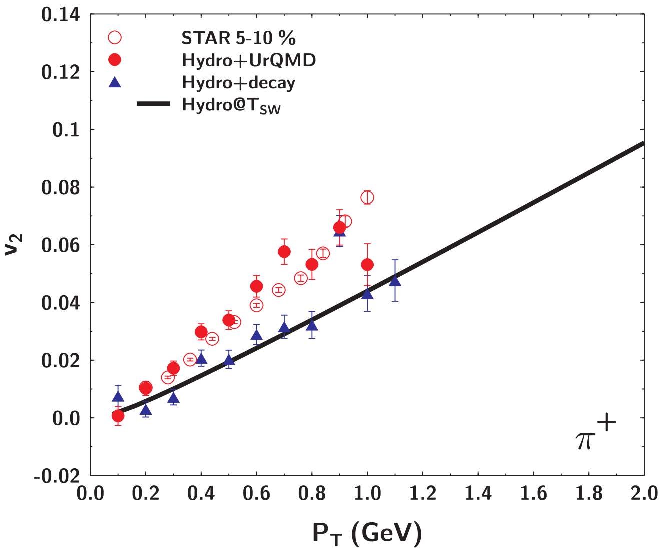

FIG. 26. (Color online) Elliptic flow as a function of P_T of π^+ at centrality 5%–10% from pure hydro at the switching temperature, hydro+decay and hydro+UrQMD. Experimental data are from STAR [76].

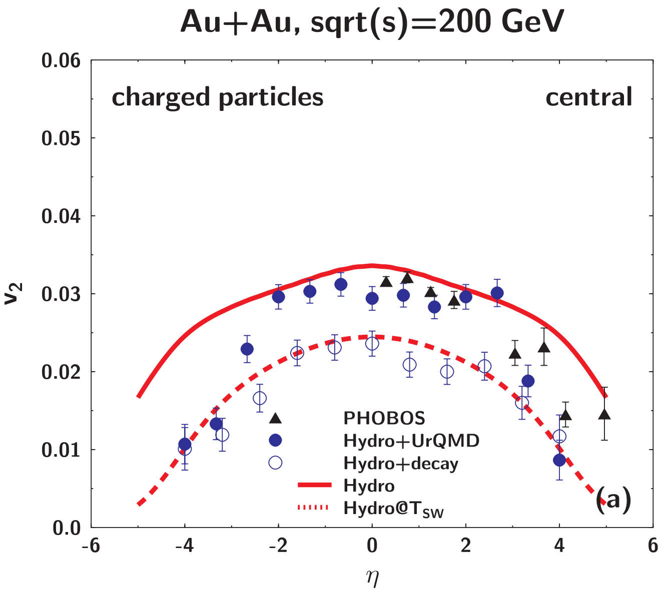

FIG. 27. (Color online) Elliptic flow as a function of η of charged particles. Solid and dashed lines stand for pure hydro calculation at the freeze-out temperature (110 MeV) and the switching temperature, respectively. Experimental data are from PHOBOS [77].

domains. As a result, the elliptic flow calculation in the hydro+micro approach is closer to the experimental data when compared with the pure hydrodynamic calculation.

IV. SUMMARY AND OUTLOOK

In summary, we developed a novel implementation of the well-known hybrid macroscopic/microscopic transport approach, combining a newly developed relativistic 3+1 dimensional hydrodynamic model for the early deconfined stage of the reaction and the hadronization process with a microscopic nonequilibrium model for the later hadronic stage at which the hydrodynamic equilibrium assumptions are no longer valid. Within this approach, we have dynamically calculated the freeze-out of the hadronic system, accounting for the collective flow on the hadronization hypersurface generated by the QGP expansion. We have compared against experimental data the results of our hybrid model and those of a calculation utilizing our hydrodynamic model for the full evolution of the reaction. This comparison has allowed us to quantify the strength of dissipative effects prevalent in the later hadronic phase of the reaction, which cannot be properly treated in the framework of ideal hydrodynamics.

Our calculations confirm those made by previous hydro+micro model implementations in 1+1 and 2+1 dimensions [15,16], demonstrating the robustness of the hydro+micro approach across different implementations of the hydrodynamic model. We also note that for the description of midrapidity data at RHIC, the extension to 3+1 dimensions in the hydrodynamic component does not yield a significant change in the results regarding spectra and collective flow.

Overall, the improved treatment of the hadronic phase provides a far better agreement between transport calculation and data, in particular concerning the flavor dependence of radial flow observables and the collective behavior of matter at forward/backward rapidities compared to ideal hydrodynamics. We find that the hadronic phase of the heavy-ion reaction at top RHIC energy is of significant duration (at least 10 fm/c) and that hadronic freeze-out is a continuous process, strongly dependent on hadron flavor and momenta.

With this work we have established a baseline—both for the regular 3+1 dimensional hydrodynamic model and for the hybrid hydro+micro approach. In forthcoming publications, we shall expand on this baseline by investigating the effects of a realistic lattice-QCD motivated equation of state containing a tri-critical point and by performing an analysis of two particle correlations (HBT interferometry). We also plan to use our model as the medium for the propagation of jets and heavy quarks and to study the modification of our medium caused by the passage of these hard probes.

ACKNOWLEDGMENTS

We thank Berndt Mueller and Ulrich Heinz for many valuable discussions and Berndt Mueller for the careful reading of this manuscript. This work was supported by an Outstanding Junior Investigator Award under Grant No. DE-FG02-03ER41239 and by a Japan Society for the Promotion of Science Postdoctoral Fellowship for Research Abroad.

APPENDIX

Equation (1) in (τ, x, y, η) is written in the following explicit way:

$$
\begin{pmatrix}
\tilde{\gamma}^2\tilde{v}_x & \tilde{\gamma}^2\tilde{v}_y & \tilde{\gamma}^2\tilde{v}_\eta & \frac{1}{\omega}\frac{d\epsilon}{dT} & \frac{1}{\omega}\frac{d\epsilon}{d\mu} \\
\tilde{\gamma}^2 & 0 & 0 & \frac{1}{\omega}\tilde{v}_x\frac{dp}{dT} & \frac{1}{\omega}\tilde{v}_x\frac{dp}{d\mu} \\
0 & \tilde{\gamma}^2 & 0 & \frac{1}{\omega}\tilde{v}_y\frac{dp}{dT} & \frac{1}{\omega}\tilde{v}_y\frac{dp}{d\mu} \\
0 & 0 & \tilde{\gamma}^2 & \frac{1}{\omega}\tilde{v}_\eta\frac{dp}{dT} & \frac{1}{\omega}\tilde{v}_\eta\frac{dp}{d\mu} \\
n_B\tilde{\gamma}^2\tilde{v}_x & n_B\tilde{\gamma}^2\tilde{v}_y & n_B\tilde{\gamma}^2\tilde{v}_y & \frac{dn_B}{dT} & \frac{dn_B}{d\mu}
\end{pmatrix}
\partial_\tau
\begin{pmatrix} \tilde{v}_x \\ \tilde{v}_y \\ \tilde{v}_\eta \\ T \\ \mu \end{pmatrix}
$$

$$
+ \begin{pmatrix}
\tilde{\gamma}^2\tilde{v}_x^2 + 1 & \tilde{\gamma}^2\tilde{v}_x\tilde{v}_y & \tilde{\gamma}^2\tilde{v}_x\tilde{v}_\eta & \frac{1}{\omega}\tilde{v}_x\frac{d\epsilon}{dT} & \frac{1}{\omega}\tilde{v}_x\frac{d\epsilon}{d\mu} \\
\tilde{\gamma}^2\tilde{v}_x & 0 & 0 & \frac{1}{\omega}\frac{dp}{dT} & \frac{1}{\omega}\frac{dp}{d\mu} \\
0 & \tilde{\gamma}^2\tilde{v}_x & 0 & 0 & 0 \\
0 & 0 & \tilde{\gamma}^2\tilde{v}_x & 0 & 0 \\
n_B\left(\tilde{\gamma}^2\tilde{v}_x^2 + 1\right) & n_B\tilde{\gamma}^2\tilde{v}_x\tilde{v}_y & n_B\tilde{\gamma}^2\tilde{v}_x\tilde{v}_\eta & \tilde{v}_x\frac{dn_B}{dT} & \tilde{v}_x\frac{dn_B}{d\mu}
\end{pmatrix}
$$

$$
\times \partial_x \begin{pmatrix} \tilde{v}_x \\ \tilde{v}_y \\ \tilde{v}_\eta \\ T \\ \mu \end{pmatrix}
$$

$$
+ \begin{pmatrix}
\tilde{\gamma}^2\tilde{v}_y\tilde{v}_x & \tilde{\gamma}^2\tilde{v}_y^2 + 1 & \tilde{\gamma}^2\tilde{v}_y\tilde{v}_\eta & \frac{1}{\omega}\tilde{v}_y\frac{d\epsilon}{dT} & \frac{1}{\omega}\tilde{v}_y\frac{d\epsilon}{d\mu} \\
\tilde{\gamma}^2\tilde{v}_y & 0 & 0 & 0 & 0 \\
0 & \tilde{\gamma}^2\tilde{v}_y & 0 & \frac{1}{\omega}\frac{dp}{dT} & \frac{1}{\omega}\frac{dp}{d\mu} \\
0 & 0 & \tilde{\gamma}^2\tilde{v}_y & 0 & 0 \\
n_B\tilde{\gamma}^2\tilde{v}_x\tilde{v}_y & n_B\left(\tilde{\gamma}^2\tilde{v}_y^2 + 1\right) & n_B\tilde{\gamma}^2\tilde{v}_y\tilde{v}_\eta & \tilde{v}_y\frac{dn_B}{dT} & \tilde{v}_y\frac{dn_B}{d\mu}
\end{pmatrix}
$$

$$
\times \partial_y \begin{pmatrix} \tilde{v}_x \\ \tilde{v}_y \\ \tilde{v}_\eta \\ T \\ \mu \end{pmatrix}
$$

$$
+ \begin{pmatrix}
\tilde{\gamma}^2\tilde{v}_\eta\tilde{v}_x & \tilde{\gamma}^2\tilde{v}_\eta\tilde{v}_y & \tilde{\gamma}^2\tilde{v}_\eta^2 + 1 & \frac{1}{\omega}\tilde{v}_\eta\frac{d\epsilon}{dT} & \frac{1}{\omega}\tilde{v}_\eta\frac{d\epsilon}{d\mu} \\
\tilde{\gamma}^2\tilde{v}_\eta & 0 & 0 & 0 & 0 \\
0 & \tilde{\gamma}^2\tilde{v}_\eta & 0 & 0 & 0 \\
0 & 0 & \tilde{\gamma}^2\tilde{v}_\eta & \frac{1}{\omega}\frac{dp}{dT} & \frac{1}{\omega}\frac{dp}{d\mu} \\
n_B\tilde{\gamma}^2\tilde{v}_x\tilde{v}_\eta & n_B\tilde{\gamma}^2\tilde{v}_\eta\tilde{v}_y & n_B\left(\tilde{\gamma}^2\tilde{v}_\eta^2 + 1\right) & \tilde{v}_\eta\frac{dn_B}{dT} & \tilde{v}_\eta\frac{dn_B}{d\mu}
\end{pmatrix}
$$

$$
\times \frac{1}{\tau}\partial_\eta \begin{pmatrix} \tilde{v}_x \\ \tilde{v}_y \\ \tilde{v}_\eta \\ T \\ \mu \end{pmatrix}
+ \begin{pmatrix}
\frac{1}{\tau} \\
-\frac{1}{\tau}\tilde{v}_x\tilde{v}_\eta^2\tilde{\gamma}^2 \\
-\frac{1}{\tau}\tilde{v}_y\tilde{v}_\eta^2\tilde{\gamma}^2 \\
-\frac{1}{\tau}(\tilde{\gamma}^2\tilde{v}_\eta - \tilde{v}_\eta^3\tilde{\gamma}^2) \\
\frac{1}{\tau}n_B
\end{pmatrix}
= 0, \tag{A1}
$$

where $\tilde{\gamma} = 1/\sqrt{1 - \tilde{v}_x^2 - \tilde{v}_y^2 - \tilde{v}_\eta^2}$, $Y_L = 1/2 \ln[(1 + v_z)/(1 - v_z)]$. The difference between the relativistic hydrodynamic equations in Cartesian coordinates and those in the (τ, x, y, η) coordinates is the addition of the fifth term in Eq. (A1).

[1] E. W. Kolb and M. S. Turner, *The Early Universe*, Frontiers in Physics, Vol. 69 (Addison-Wesley, Reading, MA, 1990).

[2] J. C. Collins and M. J. Perry, Phys. Rev. Lett. **34**, 1353 (1975); E. V. Shuryak, Phys. Rep. **61**, 71 (1980); K. Yagi, T. Hatsuda, and Y. Miake, *Quark-Gluon Plasma,* Cambridge Monographs on Particle Physics Nuclear Physics and Cosmology Vol. 23 (Cambridge University, Cambridge, 2005).

[3] B. B. Back *et al.* (PHOBOS Collaboration), Phys. Rev. Lett. **85**, 3100 (2000); C. Adler *et al.* (STAR Collaboration), *ibid.* **86**, 4778 (2001); K. Adcox *et al.* (PHENIX Collaboration), *ibid.* **86**, 3500 (2001); K. Adcox *et al.* (PHENIX Collaboration), *ibid.* **87**, 052301 (2001); B. B. Back *et al.* (PHOBOS Collaboration), *ibid.* **87**, 102301 (2001); C. Adler *et al.* (STAR Collaboration), *ibid.* **87**, 112303 (2001); I. G. Bearden *et al.* (BRAHMS Collaboration), *ibid.* **87**, 112305 (2001).

[4] K. H. Ackermann *et al.* (STAR Collaboration), Phys. Rev. Lett. **86**, 402 (2001); C. Adler *et al.* (STAR Collaboration), *ibid.* **87**, 182301 (2001).

[5] C. Adler *et al.* (STAR Collaboration), Phys. Rev. Lett. **87**, 082301 (2001).

[6] T. Ludlam, Nucl. Phys. **A750**, 9 (2005).

[7] M. Gyulassy and L. McLerran, Nucl. Phys. **A750**, 30 (2005).

[8] S. A. Bass, M. Gyulassy, H. Stöcker, and W. Greiner, J. Phys. G **25**, R1 (1999).

[9] J. D. Bjorken, Phys. Rev. D **27**, 140 (1983).

[10] R. B. Clare and D. Strottman, Phys. Rep. **141**, 177 (1986).

[11] A. Dumitru and D. H. Rischke, Phys. Rev. C **59**, 354 (1999).

[12] P. F. Kolb and U. W. Heinz, in *Quark-Gluon Plasma 3,* edited by R. C. Hwa and X.-N. Wang (World Scientific, Singapore, 2004), p. 634.

[13] P. Huovinen, in *Quark-Gluon Plasma 3,* edited by R. C. Hwa and X.-N. Wang (World Scientific, Singapore, 2004), p. 600.

[14] T. Hirano and K. Tsuda, Phys. Rev. C **66**, 054905 (2002).

[15] S. A. Bass and A. Dumitru, Phys. Rev. C **61**, 064909 (2000).

[16] D. Teaney, J. Lauret, and E. V. Shuryak, Phys. Rev. Lett. **86**, 4783 (2003); nucl-th/011037.

[17] T. Hirano, U. W. Heinz, D. Kharzeev, R. Lacey, and Y. Nara, Phys. Lett. **B636**, 299 (2006).

[18] S. A. Bass, M. Belkacem, M. Bleicher, M. Brandstetter, L. Bravina, C. Ernst, L. Gerland, M. Hofmann, S. Hofmann, J. Konopka, G. Mao, L. Neise, S. Soff, C. Spieles, H. Weber, L. A. Winckelmann, H. Stöcker, W. Greiner, C. Hartnack, J. Aichelin, and N. Amelin, Prog. Part. Nucl. Phys. **41**, 225 (1998); M. Bleicher, E. Zabrodin, C. Spieles, S. A. Bass, C. Ernst, S. Soff, L. Bravina, M. Belkacem, H. Weber, H. Stöcker, and W. Greiner, J. Phys. G **25**, 1859 (1999).

[19] C. Nonaka, E. Honda, and S. Muroya, Eur. Phys. J. C **17**, 663 (2000).

[20] T. Hirano, Phys. Rev. C **65**, 011901(R) (2001).

[21] P. Huovinen, Nucl. Phys. **A761**, 296 (2005).

[22] F. Karsch, J. Phys. G **31**, S633 (2005).

[23] C. Bernard, T. Burch, C. DeTar, J. Osborn, S. Gottlieb, E. B. Gregory, D. Toussaint, U. M. Heller, R. Sugar (MILC Collaboration), Phys. Rev. D **71**, 034504 (2005).

[24] M. G. Alford, K. Rajagopal, and F. Wilczek, Phys. Lett. **B422**, 247 (1998).

[25] R. Rapp, T. Schafer, E. V. Shuryak, and M. Velkovsky, Phys. Rev. Lett. **81**, 53 (1998).

[26] M. Stephanov, K. Rajagopal, and E. Shuryak, Phys. Rev. Lett. **81**, 4816 (1998).

[27] Z. Fodor and S. D. Katz, J. High Energy Phys. 03, (2002) 014.

[28] R. Gavai, S. Gupta, and R. Ray, Prog. Theor. Phys. Suppl. **153**, 270 (2004).

[29] C. R. Allton, S. Ejiri, S. J. Hands, O. Kaczmarek, F. Karsch, E. Laermann, C. Schmidt, and L. Scorzato, Phys. Rev. D **66**, 074507 (2002).

[30] M. D'Elia and M. P. Lombardo, Phys. Rev. D **67**, 014505 (2003).

[31] Z. Fodor, S. D. Katz, and K. K. Szabo, Phys. Lett. **B568**, 73 (2003).

[32] R. V. Gavai and S. Gupta, Phys. Rev. D **71**, 114014 (2005).

[33] Z. Fodor and S. D. Katz, J. High Energy Phys. 04, (2004) 050.

[34] S. Ejiri, C. R. Allton, S. J. Hands, O. Kaczmarek, F. Karsch, E. Laermann, and C. Schmidt, Prog. Theor. Phys. Suppl. **153**, 118 (2004).

[35] J. Sollfrank, P. Huovinen, M. Kataja, P. V. Ruuskanen, M. Prakash, and R. Venugopalan, Phys. Rev. C **55**, 392 (1997).

[36] C. M. Hung and E. Shuryak, Phys. Rev. C **57**, 1891 (1998).

[37] D. H. Rischke, M. I. Gorenstein, H. Stöcker, and W. Greiner, Z. Phys. C **51**, 485 (1991).

[38] U. Ornik, M. Plümer, B. R. Schlei, D. Strottman, and R. M. Weiner, Phys. Rev. C **54**, 1381 (1996); B. R. Schlei, U. Ornik, M. Plümer, D. Strottman, and R. M. Weiner, Phys. Lett. **B376**, 212 (1996); B. R. Schlei, Heavy Ion Phys. **5**, 403 (1997); N. Arbex, U. Ornik, M. Plümer, and R. M. Weiner, Phys. Rev. C **55**, 860 (1997).

[39] J. Sollfrank, P. Huovinen, and P. V. Ruuskanen, Eur. Phys. J. C **6**, 525 (1999); talk given at the ECT Workshop on Hydrodynamics for Nuclear Collisions, Trento, May 1997, nucl-th/9706012.

[40] A. Dumitru and D. H. Rischke, Phys. Rev. C **59**, 354 (1999).

[41] A. Dumitru, C. Spieles, H. Stöcker, and C. Greiner, Phys. Rev. C **56**, 2202 (1997).

[42] J. Cleymans, K. Redlich, and D. K. Srivastava, Phys. Rev. C **55**, 1431 (1997).

[43] M. Belkacem, M. Brandstetter, S. A. Bass, M. Bleicher, L. Bravina, M. I. Gorenstein, J. Konopka, L. Neise, C. Spieles, S. Soff, H. Weber, H. Stöcker, and W. Greiner, Phys. Rev. C **58**, 1727 (1998).

[44] C. Nonaka and M. Asakawa, Phys. Rev. C **71**, 044904 (2005).

[45] Y. Hama, R. P. G. Andrade, F. Grassi, O. Socolowski Jr., T. Kodama, B. Tavares, and S. S. Padula, Nucl. Phys. **A774**, 169 (2006).

[46] P. F. Kolb, U. Heinz, P. Huovinen, K. J. Eskola, and K. Tuominen, Nucl. Phys. **A696**, 197 (2001).

[47] T. Hirano and Y. Nara, Nucl. Phys. **A743**, 305 (2004).

[48] K. J. Eskola, H. Honkanen, H. Niemi, P. V. Ruuskanen, and S. S. Räsänen, Phys. Rev. C **72**, 044904 (2005).

[49] P. Huovinen, P. F. Kolb, U. Heinz, P. V. Ruuskanen, and S. A. Voloshin, Phys. Lett. **B503**, 58 (2001).

[50] S. Mrowczynski, Acta Phys. Pol. B **37**, 427 (2006).

[51] P. Jacobs and G. Cooper, nucl-ex/0008015.

[52] P. F. Kolb, J. Sollfrank, and U. Heinz, Phys. Rev. C **62**, 054909 (2000).

[53] U. Heinz and P. F. Kolb, Phys. Lett. **B542**, 216 (2002).

[54] S. S. Adler (PHENIX Collaboration), Phys. Rev. Lett. **91**, 072303 (2003).

[55] P. F. Kolb and R. Rapp, Phys. Rev. C **67**, 044903 (2003).

[56] T. Renk, Phys. Rev. C **70**, 021903(R) (2004); **69**, 044902 (2004).

[57] J-P. Blaizot and J-Y. Ollitrault, in *Quark-Gluon Plasma*, Advanced Series on Directions in High Energy Physics Vol. 6, edited by R. C. Hwa (World Scientific, Singapore, 1990), p. 393.

[58] F. Cooper and G. Frye, Phys. Rev. D **10**, 186 (1974).

[59] Y. Yariv and Z. Fraenkel, Phys. Rev. C **20**, 2227 (1979); J. Cugnon, *ibid.* **22**, 1885 (1980); Y. Pang, T. J. Schlagel, and S. H. Kahana, Phys. Rev. Lett. **68**, 2743 (1992).
[60] H. Kruse, B. V. Jacak, and H. Stöcker, Phys. Rev. Lett. **54**, 289 (1985); J. Aichelin and G. Bertsch, Phys. Rev. C **31**, 1730 (1985); J. J. Molitoris and H. Stöcker, *ibid.* **32**, R346 (1985); K. Weber, B. Blattel, V. Koch, A. Lang, W. Cassing, and U. Mosel, Nucl. Phys. **A515**, 747 (1990); B. A. Li and C. M. Ko, Phys. Rev. C **52**, 2037 (1995); W. Ehehalt and W. Cassing, Nucl. Phys. **A602**, 449 (1996).
[61] J. Aichelin, A. Rosenhauer, G. Peilert, H. Stoecker, and W. Greiner, Phys. Rev. Lett. **58**, 1926 (1987); G. Peilert, H. Stöcker, W. Greiner, A. Rosenhauer, A. Bohnet, and J. Aichelin, Phys. Rev. C **39**, 1402 (1989); H. Sorge, H. Stöcker, and W. Greiner, Ann. Phys. (NY) **192**, 266 (1989); J. Aichelin, Phys. Rep. **202**, 233 (1991).
[62] B. Andersson, G. Gustafson, G. Ingelman, and T. Sjöstrand, Phys. Rep. **97**, 31 (1983); B. Andersson, G. Gustafson, and B. Nilsson-Almqvist, Nucl. Phys. **B281**, 289 (1987).
[63] F. Laue *et al.*, Phys. Rev. Lett. **82**, 1640 (1999); W. Chang *et al.*, in *Proceedings of the 15th Winter Workshop on Nuclear Dynamics, Park City, UT, January 1999*, nucl-ex/9904010.
[64] R. M. Barnett *et al.* (Particle Data Group), Phys. Rev. D **54**, 1 (1996).
[65] P. Danielewicz and G. F. Bertsch, Nucl. Phys. **A533**, 712 (1991).
[66] S. S. Adler *et al.* (PHENIX Collaboration), Phys. Rev. C **69**, 034909 (2004).
[67] M. Estienne (STAR Collaboration), J. Phys. G **31**, S873 (2005).
[68] U. Heinz and P. F. Kolb, in 18th Winter Workshop on Nuclear Dynamics, Nassau, Bahama, January 2002; P. Huovinen, Nucl. Phys. **A715**, 299c (2003).
[69] D. Teaney, nucl-th/0204023.
[70] K. Adcox *et al.* (PHENIX collaboration), Nucl. Phys. **A757**, 184 (2004).
[71] B. B. Back *et al.* (PHOBOS Collaboration), Phys. Rev. Lett. **91**, 052303 (2003).
[72] T. Hirano, K. Morita, S. Muroya, and C. Nonaka, Phys. Rev. C **65**, 061902 (2005); K. Morita, S. Muroya, C. Nonaka, and T. Hirano, *ibid.* **66**, 054904 (2002).
[73] J. Adams *et al.* (STAR Collaboration), Phys. Rev. C **72**, 014904 (2005).
[74] B. B. Back *et al.* (PHOBOS Collaboration), Phys. Rev. C **72**, 051901(R) (2005).
[75] R. Rapp and E. V. Shuryak, Phys. Rev. Lett. **86**, 2980 (2001).
[76] C. Greiner and S. Leupold, J. Phys. G **27**, L95 (2001).
[77] J. Adames *et al.* (STAR Collaboration), Phys. Rev. Lett. **92**, 182301 (2004).
[78] H. van Hecke, H. Sorge, and N. Xu, Phys. Rev. Lett. **81**, 5764 (1998).
[79] A. Dumitru, S. A. Bass, M. Bleicher, H. Stoecker, and W. Greiner, Phys. Lett. **B460**, 411 (1999).
[80] P. G. Jones and the NA49 Collaboration, Nucl. Phys. **A610**, 188c (1996); C. Bormann *et al.* (NA49 Collaboration), J. Phys. G **23**, 1817 (1997); H. Appelshäuser *et al.* (NA49 Collaboration), Phys. Lett. **B444**, 523 (1998); E. Andersen *et al.* (WA97 Collaboration), *ibid.* **B433**, 209 (1998); E. Andersen *et al.* (WA97 Collaboration), J. Phys. G **25**, 181 (1999).
[81] H. Sorge, Phys. Rev. Lett. **78**, 2309 (1997).
[82] J. Adams *et al.* (STAR Collaboration), Phys. Rev. Lett. **92**, 052302 (2004).
[83] D. Molnar and S. A. Voloshin, Phys. Rev. Lett. **91**, 092301 (2003).